Insights into the Evolving Microphysical and Kinematic Structure of Northeastern U.S. Winter Storms from Dual-Polarization Doppler Radar

MATTHEW R. KUMJIAN

Department of Meteorology and Atmospheric Science, The Pennsylvania State University, University Park, Pennsylvania

KELLY A. LOMBARDO

Department of Marine Sciences, University of Connecticut, Avery Point, Connecticut

(Manuscript received 24 December 2015, in final form 2 December 2016)

ABSTRACT

The recent Weather Surveillance Radar-1988 Doppler (WSR-88D) network upgrade to dual-polarization capabilities allows for bulk characterization of microphysical processes in northeastern U.S. winter storms for the first time. In this study, the quasi-vertical profile (QVP) technique (wherein data from a given elevation angle scan are azimuthally averaged and the range coordinate is converted to height) is extended and applied to polarimetric WSR-88D observations of six Northeast winter storms to survey their evolving, bulk vertical microphysical and kinematic structures. These analyses are supplemented using hourly analyses from the Rapid Refresh (RAP) model. Regions of ascent inferred from QVPs were consistently associated with notable polarimetric signatures, implying planar crystal growth when near −15°C, and riming and secondary ice production at higher temperatures. The heaviest snowfall occurred most often when ascent and enhanced propagation differential phase shift (Φ_{DP}) occurred near −15°C. When available, limited surface observations confirmed heavy snowfall rates and revealed large snow-to-liquid ratios at these times. Other cases revealed sudden, large melting-layer excursions associated with precipitation-type transitions near the surface. RAP analyses failed to capture such complex evolution, demonstrating the added value of dual-polarization radar observations in these scenarios and the potential use of radar data for assessing model performance in real time. These insights are a preliminary step toward better understanding the complex processes in northeastern U.S. winter storms.

1. Introduction

According to the U.S. Census Bureau, more than 56 million people live in the northeastern United States, the vast majority of which live along a coastal corridor extending from Washington, D.C., to Boston, Massachusetts. This is the most heavily urbanized region in the United States, containing major economic and cultural centers, as well as essential transportation routes and hubs. Cold-season extratropical cyclones along the northeastern U.S. coast can produce debilitating snowfall accumulations and mixed-phase precipitation in these major metropolitan areas, disrupting transportation, commerce, and society (e.g., Kocin and Uccellini 2004 and references therein). Further, intense coastal lows often produce high winds and waves that can damage coastal structures (Picca et al. 2014). Recent blizzards labeled as "historic" have individually cost tens of millions of dollars in damage and significant loss of life (e.g., Griffin et al. 2014; Picca et al. 2014). Even when major cities are spared the extreme weather, there can be an enormous economic toll: an estimated $200 million was lost in January 2015 when New York City (NYC) shut down its transit system based on forecasts of a major snow event (Dokoupil 2015). During that event, the forecasted snowfall totals for NYC did not verify.[1] Given the predicted increase in cool-season

Supplemental information related to this paper is available at the Journals Online website: http://dx.doi.org/10.1175/MWR-D-15-0451.s1.

Corresponding author e-mail: Dr. Matthew R. Kumjian, kumjian@psu.edu

[1] Though several tens of kilometers east of NYC, in eastern Long Island, enormous snowfall totals did verify. If NYC did receive what was forecasted, the economic and societal toll on the city surely would have been much larger.

DOI: 10.1175/MWR-D-15-0451.1

precipitation from northeastern U.S. cyclones over the next century (e.g., Lombardo et al. 2015), a better understanding of processes contributing to heavy snow production and attendant hazards is critical to better anticipate and prepare for such events.

In part, forecast errors and uncertainties arise owing to a complex interplay of dynamic, thermodynamic, and microphysical processes acting at a range of scales that may not be adequately represented in numerical weather prediction models. For example, heating owing to cloud and precipitation microphysical processes is thought to play an important role in the formation and intensification of cyclones (e.g., Kuo and Reed 1988; Davis 1992; Posselt and Martin 2004) and their mesoscale precipitation features (e.g., Brennan and Lackmann 2005; Novak et al. 2009; Ganetis and Colle 2015). Microphysical processes also play a substantial role in determining the intensity, type, and spatial distribution of precipitation in coastal winter cyclones. Furthermore, the temperature at which ascent occurs dictates the crystal habits produced (e.g., Auer and White 1982; Bailey and Hallett 2009); the resulting snow-to-liquid ratios at the surface are strongly dependent on these crystal habits and aggregation efficiencies (Roebber et al. 2003).

Despite the importance of microphysical processes in these storms, there have been only a limited number of efforts to observationally characterize coastal winter storm microphysics. Recent work by Stark et al. (2013) was the first to document the microphysical evolution observed at the surface during two cyclones. Using a vertically pointing Micro Rain Radar (MRR; Peters et al. 2002) in conjunction with crystal habit and riming classifications at ground level, the authors highlight large variations in habit, riming, and precipitation intensity throughout the two events. To see if such variability could be anticipated from operational models, they inspected 13-km Rapid Update Cycle (RUC; Benjamin et al. 2004) data; they suggest that the model resolution was too coarse to capture the environmental variations that would support the observed microphysical evolution. In a follow-up study of more cases, Colle et al. (2014) found multiple habits reaching the surface contemporaneously, highlighting the microphysical complexity in these storms. However, both studies only examined data from a single location, lacking information about ongoing microphysical processes aloft and elsewhere in the storm.

In contrast, dual-polarization radar data can provide information about the bulk microphysical structure in storms across a larger areal extent. However, to date only three studies have used dual-polarization radar data to explore the microphysical structure of northeastern coastal winter storms (Griffin et al. 2014; Picca et al. 2014; Ganetis and Colle 2015). Griffin et al. (2014) analyze polarimetric radar data in the historic 8–9 February 2013 storm, which ranks among the top five worst the northeastern United States has experienced. The authors highlight a number of signatures associated with precipitation transitions, vigorous dendritic growth, and even a flarelike echo resembling a three-body scattering signature. Picca et al. (2014) studied the same storm, focusing on the operational utility of dual-polarization radar observations for real-time precipitation transition zone identification, forecasting, and emergency management operations. Importantly, the polarimetric radar data helped reconcile seemingly conflicting observations (of reduced reflectivity factor within a band in which snowfall rates remained large) by providing forecasters with some information about the type of particles found within the band: in this case, the transition represented a change from high-density hydrometeors to low-density snow aggregates. Finally, Ganetis and Colle (2015) also studied the 8–9 February 2013 blizzard, but from a modeling perspective. In their study, dual-polarization radar data are used to qualitatively assess the model performance and provide context for the evolution of the observed snowband.

These studies identified new and useful signatures that currently lack well-developed explanations and highlight the utility of dual-polarization radar data for operational applications. This includes regions of large reflectivity factor (>50 dBZ) associated with wet snow and high-density hydrometeors, abrupt transitions in the surface precipitation type, and crystal growth zones aloft. However, all investigated *the same storm using the same dataset* from the polarimetric WSR-88D near Upton, New York. Clearly, investigations of more cases are needed to determine the repeatability of the documented signatures, understand their underlying causes, and provide more robust microphysical insights into the nature of these storms. Further, detection of enhanced precipitation rates is of critical importance for short-term forecasts of snowfall accumulations, so identifying and understanding operationally useful signatures is of value.

The purpose of this study is to survey dual-polarization Doppler WSR-88D observations of a number of northeastern U.S. winter storms in order to gain insights into their evolving microphysical structure. A detailed analysis of finescale microphysical structures in northeastern U.S. winter storms is beyond the scope of this paper, given the large number of long-duration (sometimes >24 h) events. Instead, we adopt a technique to provide insights into the evolving bulk, repeatable structures. Though this facilitates investigation

TABLE 1. List of cases analyzed for this study and the radars used for the analysis.

Date	WSR-88D
19–20 Dec 2009	KOKX
8–9 Feb 2013	KOKX
15–16 Feb 2014	KBOX
24–25 Jan 2015	KBOX, KOKX
26–28 Jan 2015	KBOX, KOKX
5–6 Mar 2015	KOKX

of a larger number of cases, it sacrifices more detailed analyses. As such, this study should be seen as a first step toward characterizing microphysical and kinematic structures in northeastern U.S. winter storms, perhaps providing a roadmap for future, more detailed analyses.

In our analyses, we find a number of consistent, reliable polarimetric and Doppler signatures related to microphysical, thermodynamic, and kinematic processes within these storms. The following section provides an overview of the data and methods used in the analysis, the results of which are presented in section 3. A discussion and summary of the conclusions is found in section 4.

2. Data and methods

a. Datasets

1) DUAL-POLARIZATION WSR-88D DATA

Table 1 provides a list of the northeastern winter storms analyzed in this study. All but the first of these storms occurred after the WSR-88Ds used were upgraded to dual-polarization capabilities. These radars include the one near Upton (KOKX) and Boston (KBOX). The first storm was studied previously (Stark et al. 2013; Colle et al. 2014) and thus is presented to demonstrate the technique used herein and to compare methodologies in the following subsection. Though we investigated all northeastern winter cyclones in 2014/15 with good coverage by the WSR-88Ds (after the dual-polarization upgrade was completed), the subset of cases presented herein are chosen for their exemplary or unique aspects. Many of the storms exhibited similar features to those presented herein. For each case, level II data from the National Centers for Environmental Information (NCEI) are used instead of level III data, primarily for the availability of scans at higher antenna elevation angles. Radar variables available from level II data used include the radar reflectivity factor at horizontal polarization Z_H, Doppler velocity V_R, differential reflectivity Z_{DR}, propagation differential phase shift Φ_{DP}, and the copolar correlation coefficient ρ_{hv} (or CC), which is available at all tilts; level III data include processed K_{DP} instead of Φ_{DP} and only include the lowest tilts. Data with $Z_H < -10$ dBZ are censored in an effort to mitigate biases from low signal-to-noise ratio. No ρ_{hv} thresholds were applied, in order to preserve melting-layer signatures and those from potentially useful signatures such as the "snow flare." For details about the polarimetric radar variables and their physical interpretation, see reviews by Doviak and Zrnić (1993), Zrnić and Ryzhkov (1999), Bringi and Chandrasekar (2001), Ryzhkov et al. (2005), and Kumjian (2013a,b,c).

2) RAPID REFRESH MODEL ANALYSES

Supplementary thermodynamic and kinematic information is available from hourly analyses by the operational Rapid Refresh model, the newest generation of the RUC model. The RAP has 50 vertical levels and 13-km horizontal grid lengths over North America. Specifically, vertical profiles of temperature and pressure vertical velocity ($\omega = \partial p/\partial t$) at the grid boxes nearest the WSR-88Ds are used. These data were downloaded from NCEI where available. In the absence of RAP data, data from standard radiosonde launches are used. According to the RAP website (http://rapidrefresh.noaa.gov), a major system upgrade occurred in 2014, which (among other things) improved the radar reflectivity factor data assimilation and cloud analysis. It is important to keep these upgrades in mind when comparing model analyses of cases before and after 2014.

3) OTHER DATA SOURCES

Some cases are supplemented by additional surface observations from a variety of sources. Data from previously published studies are used when available. Automated Surface Observing System (ASOS; e.g., Ryerson and Ramsay 2007) data are used to demonstrate hourly snowfall rates. The ASOSs used herein provide basic sky conditions, visibility, present weather, state variables, and automated precipitation-type identification. Citizen-submitted precipitation-type reports as part of the mobile Precipitation Identification Near the Ground (mPING; Elmore et al. 2014) project are used qualitatively to increase confidence in METAR precipitation-type reports.

b. Methods

The data analysis technique adopted for this study is to construct quasi-vertical profiles (QVPs) of the radar variables (Kumjian et al. 2013; Trömel et al. 2013; Ryzhkov et al. 2016; Kumjian et al. 2016; Oue et al. 2016; Van den Broeke et al. 2016). QVPs are constructed via azimuthally averaging data collected at high (≥10°)

fixed-antenna-elevation angles and converting the range coordinate to height. Thus, QVP geometry favors vertical resolution at the expense of horizontal resolution, particularly at higher altitudes (larger ranges). In the absence of high-resolution, volumetric radar coverage, we argue that this averaging technique provides useful insights into the bulk vertical precipitation structure of widespread storms, even those that exhibit horizontal heterogeneities. Though such averaging tends to smooth out finescale horizontal structures, the averaging also reduces noise in radar moment estimates. Because the standard deviation of moments like Z_{DR} and Φ_{DP} are proportional to $M^{-1/2}$, where M is the number of samples (e.g., Melnikov 2004), averaging over 360 azimuths reduces the variability by a factor of $360^{1/2}$ (Ryzhkov et al. 2016). The effective vertical resolution afforded by QVPs is superior to other binning techniques, but degrades with altitude owing to beam broadening (Ryzhkov et al. 2016). For example, it is ~100 m at 1-km altitude, but degrades to ~800 m at 9 km, which is the maximum height shown in this analysis.

Herein, the 10° elevation angle scan is used when available; otherwise, the analysis defaults to the highest available elevation angle. This angle was selected based on considerations of different factors including vertical resolution, averaging over a small domain, velocity contributions from hydrometeor fall speeds, and the ability to sample low levels. Sensitivity tests (see the appendix) indicated that bulk features were indistinguishable when comparing elevation angles between 10° and 19.5°, the highest elevation angle available in the operational dataset. A single QVP is constructed from each volume scan, with temporal resolution ranging from ~5 to ~10 min depending on the operational scanning strategy employed. We computed K_{DP} as follows. First, the Φ_{DP} QVP was smoothed with a 15-gate boxcar filter. Then, a line was fit to the smoothed profile using a 9-gate moving window, where K_{DP} is half the slope of this linear fit. The K_{DP} data are censored if <360° are included in the azimuthal averaging.

Consecutive QVPs are collated to provide a time–height analysis of polarimetric and Doppler radar variables. The resulting plots provide clear depictions of the evolving bulk vertical microphysical structure on scales comparable to grid spacings in mesoscale numerical weather prediction (NWP) models, facilitating comparisons with such models. In addition, V_R QVPs provide an estimate of the mesoscale divergence/convergence ($\overline{\delta}$) and thus implied vertical motion over the radar site (see the appendix). Briefly, net convergence (divergence) into the conical scan region averaged for the QVP results in net negative (positive) V_R at a given height. Though hydrometeor vertical velocities also contribute to the net V_R QVP, it is expected that most hydrometeor fall speeds in winter storms associated with snow and ice are less than 1–2 m s^{-1} and thus are of secondary importance for the 10° scans used in this study. Regions of rain, which violate this fall speed assumption, are covered in gray shading in our images. Though V_R and $\overline{\delta}$ QVPs provide the same informative content, $\overline{\delta}$ allows for easier interpretation.

When available, operational soundings from KOKX and Chatham, Massachusetts (KCHH), are used to identify layers of significant veering for comparison with the $\overline{\delta}$ QVPs from KOKX and KBOX, respectively. According to the thermal wind relation, veering of the geostrophic winds in a layer implies warm-air advection into that layer (e.g., Bluestein 1992); this warm-air advection is quasigeostrophically associated with rising motion. Layers are identified as consecutive sounding observation points with continuous veering according to the following criteria: total veering must be >25°, layers must be >100 m deep, and layers must be separated by >100 m of no veering (i.e., backing or zero change in wind direction) to count as distinct. These layers are marked using green brackets in the $\overline{\delta}$ QVP figures herein. Veering layers are not plotted if no echo exists. Keep in mind that low-level (<1 km) veering layers likely do not correspond to ascent given the impact of surface drag (i.e., the flow is not in geostrophic balance).

To demonstrate the advantages of the QVP technique, we compare our results to those for a historical case studied by Stark et al. (2013) and Colle et al. (2014). Stark et al. (2013) provide detailed observations of the microphysical structure of the 19–20 December 2009 cyclone as observed at the surface. As part of their analysis, they show a comparison between the KOKX radar and vertically pointing MRR, reproduced here: Fig. 1a is their time–height presentation of KOKX Z_H, and Fig. 1b is the analogous data from the MRR. Figure 1c shows the same KOKX data, but presented as a Z_H QVP. The QVP method provides better vertical resolution and coverage than the binning method used in Stark et al. (2013); however, given the different sampling geometries (Fig. 1d) and that the QVP is a spatial average, the horizontal heterogeneities are considerably smoothed. Perhaps most striking is the comparable detail in the QVP to the MRR, given the areal averaging used to construct the QVP. For example, individual fall streaks are identifiable in both panels (e.g., ~1700, 1900–2000, 2100–2200 UTC, etc.). Spatially small features such as convective cells are captured in the MRR but not the QVP. However, the S-band data are less attenuated and (postupgrade) provide polarimetric insights unavailable from vertically pointing radars.

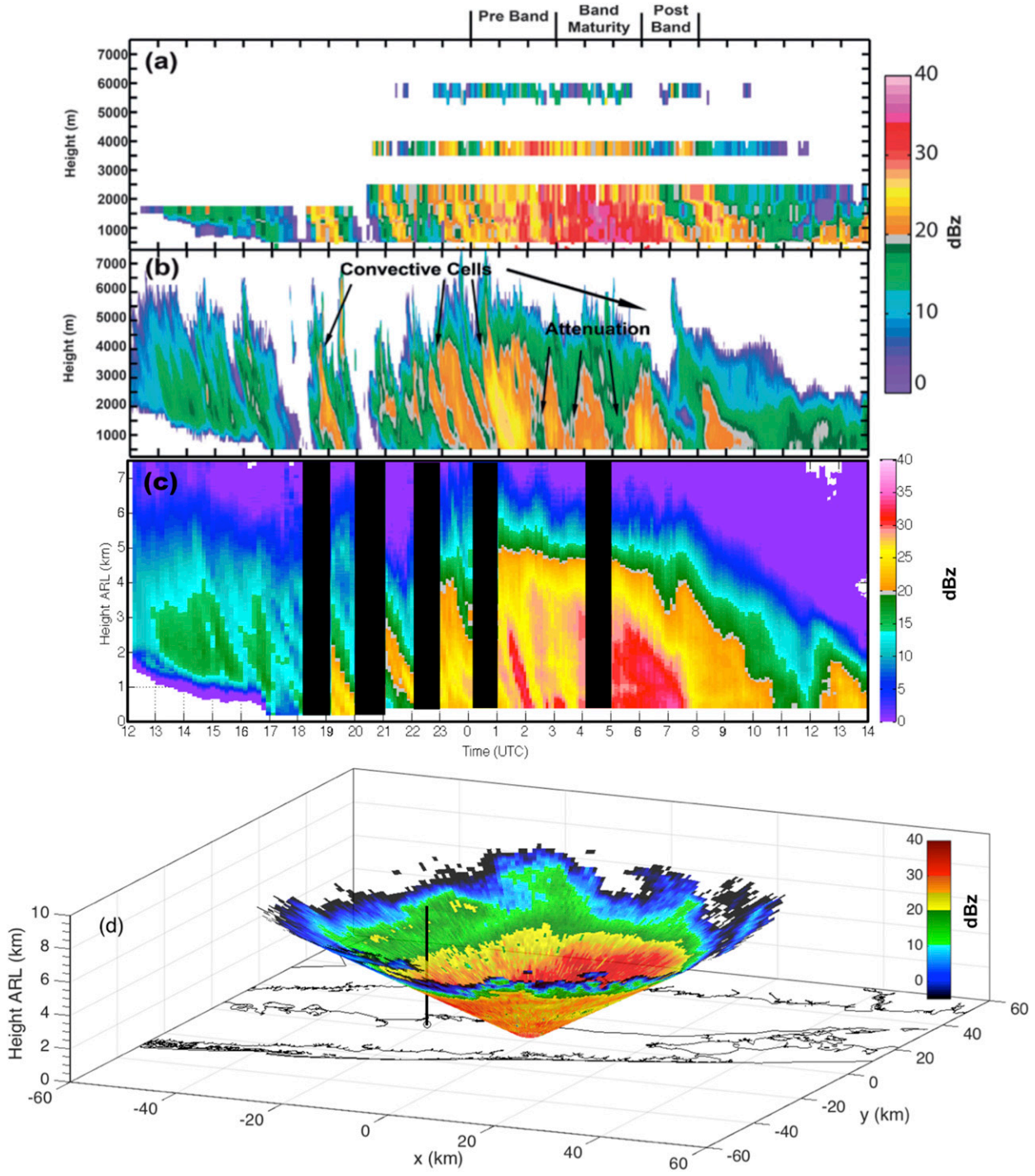

FIG. 1. (a) Time–height plot of KOKX Z_H (shaded in dBZ, according to scale), and (b) MRR equivalent reflectivity factor (shaded in dBZ) from 1200 UTC 19 Dec through 1400 UTC 20 Dec 2009, from Stark et al. (2013). (c) QVP of KOKX Z_H (shaded in dBZ according to scale) for the same time period. Vertical black bars denote missing level II data. (d) Geometry of the two radars with a map underlaid: the KOKX QVP is shown in three dimensions (dBZ shaded according to scale), and the MRR sampling region is shown by the vertical black line. KOKX is at the origin of the coordinate system and the MRR location is shown by a circle.

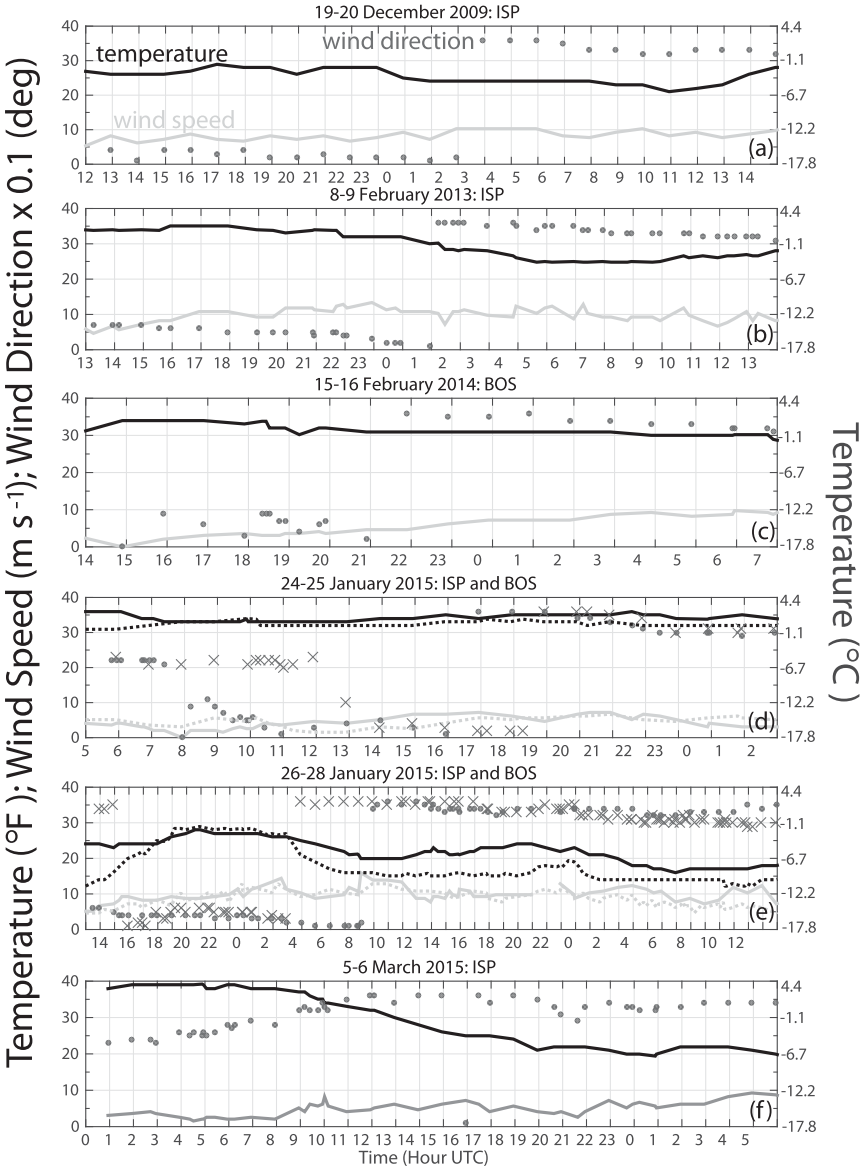

FIG. 2. Time series of ASOS observations from ISP or BOS, as applicable for each of the events. The black lines show temperature in °F, gray shows wind speed ($m\,s^{-1}$), and markers indicate wind direction (in °, scaled by a factor of 0.1 for graphical purposes). For events in which two stations are presented, KBOS is shown with dashed lines and × markers. Temperatures in °C are shown on the right ordinate axis for reference.

3. Analysis

To provide context for the subsequent QVPs, Fig. 2 shows time series from ASOS stations at Long Island MacArthur Airport [known as Islip Airport (ISP)] on Long Island, New York, or Boston's Logan International Airport (BOS), as applicable. In each case except 5–6 March 2015, the time series reveal the expected surface response to a coastal low, with winds gradually backing from northeasterly to northwesterly and steady or declining temperatures. A brief synoptic overview of each case will be provided in the beginning of each subsection. In addition, we present a series of snapshots of the storms as they produced heavy snowfall over the radar location (Fig. 3).[2] The range rings correspond to ranges at which the beam height is 2, 4, 6, 8, and 10 km above radar level in the subsequent QVPs

[2] Images available in the online supplement material show an overview surface analysis and infrared satellite image for each case at the nearest available time to those shown in Fig. 3.

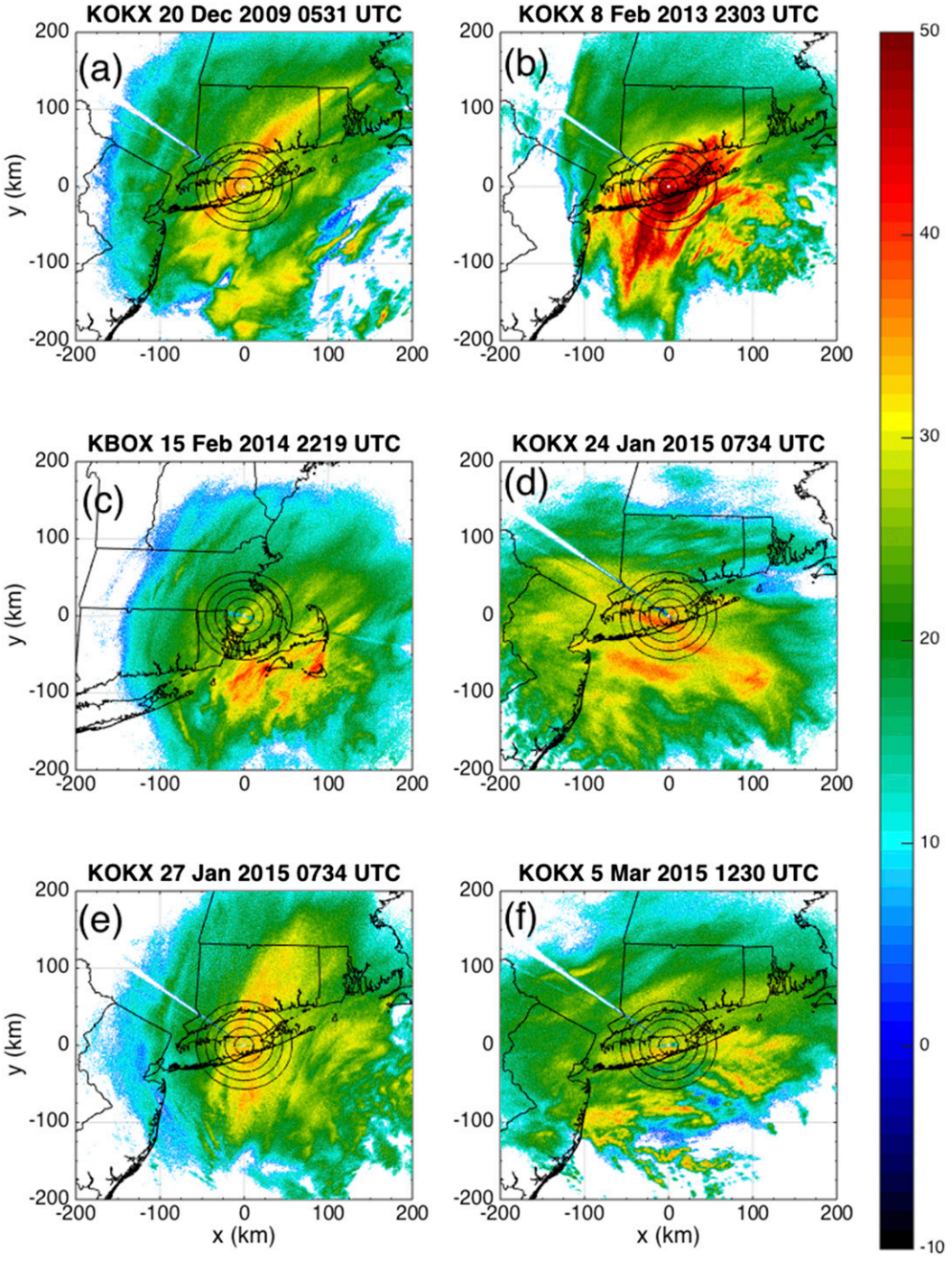

FIG. 3. A 0.5° PPI scan of Z_H (dBZ, shaded according to scale) for (a) 0531 UTC 20 Dec 2009, (b) 2303 UTC 8 Feb 2013, (c) 2219 UTC 15 Feb 2014, (d) 0734 UTC 24 Jan 2015, (e) 0734 UTC 27 Jan 2015, and (f) 1230 UTC 5 Mar 2015. Range rings indicate 2-, 4-, 6-, 8-, and 10-km beam heights for the 10° QVPs.

(i.e., beam heights are calculated using a 10°-elevation angle). In most of the cases, well-defined, narrow enhanced precipitation bands are evident. Most notably, the 8–9 February storm's precipitation band features Z_H >50 dBZ. In the other cases, the heaviest snow exhibits Z_H exceeding 30–35 dBZ. The 20 December 2009, 8–9 February 2013, and 24 and 27 January 2015 cases (Figs. 3a,b,d,e) in particular feature bands directly over the radar site at the times shown, indicating that QVPs for these cases may better reflect the microphysics

and kinematics of snowbands than the other cases. In the following subsections, not every figure shows the same polarimetric variables in order to focus on the features of interest for a given storm.

a. 19–20 December 2009

Though the 19–20 December 2009 case occurred prior to the dual-polarization upgrade, the data are still useful within the context of the detailed analysis by Stark et al. (2013). At 0000 UTC 19 December, the Weather Prediction Center (WPC) analyzed a 997-hPa surface low over southern Georgia. As this low moved offshore, it subsequently intensified and moved up the coast. By 1200 UTC, its pressure dropped to 986 hPa and it was centered over the Outer Banks of North Carolina. It continued intensifying as it moved northeastward past Long Island and Cape Cod, moving to off the southeast coast of Nova Scotia by 0000 UTC 21 December. Long Island was in the comma head of the cyclone in the early hours of 20 December, when an intense mesoscale snowband was situated over the KOKX radar (Fig. 3a). No surface frontal passages were analyzed during this event; temperatures held steady throughout the analysis period as winds gradually backed from northeasterly to northwesterly (Fig. 2a). Thus, QVPs are not expected to be biased by sharp gradients between different air masses.

Figure 4 shows Z_H, V_R (masked where $<360°$ are included in the averaging; see the appendix), and $\overline{\delta}$ QVPs for this case, with RAP analysis data overlaid. Note that these RAP analyses predate the upgrade. The largest Z_H values begin after 0000 UTC (Fig. 4a), and especially after 0300 UTC, the period that Stark et al. (2013) classify as ''band maturity.'' During this time, enhanced RAP-analyzed vertical motion exists, roughly centered on the −15°C level. Interestingly, the V_R and $\overline{\delta}$ QVPs (Figs. 4b,c) reveal a change in height of implied ascent regions: from just under 4 km between 2300 UTC 19 December and 0000 UTC 20 December to just under 5 km after 0100 UTC. This later ascent is in the vicinity of the RAP-analyzed −15°C level and is temporally offset from the enhancement in the RAP-analyzed vertical motion field, which maximizes prior to 0300 UTC. Maximum Z_H observed at low levels occurred between 0200 and 0800 UTC, during which the primary snowband was situated over KOKX (cf. Fig. 3a). The radar-inferred ascent timing and magnitudes thus appear to be more consistent with the observed Z_H evolution than the model analyses. At 0000 UTC, three sounding-observed veering layers are present. The two aloft encompass radar-inferred convergence (divergence) in the lower (upper) portion of the layer, showing some degree of consistency.

Auer and White (1982) found that heavy snow episodes tended to have the strongest large-scale ascent near −15°C. Ascent near −15°C is favorable for dendritic crystal growth, which requires large ice supersaturations (e.g., Bailey and Hallett 2009). Owing to their intricate branching structure, dendrites are very efficient aggregators at temperatures between −15° and −10°C (e.g., Lamb and Verlinde 2011). Such efficient aggregation leads to heavier snowfall and larger, fluffier aggregates that tend to produce larger snow-to-liquid ratios (SLRs) at the surface than denser, more compact snow crystals and smaller aggregates (e.g., Roebber et al. 2003). Indeed, Stark et al. (2013) found the largest SLRs (11:1 to 13:1) and a dominance of dendritic crystals at the surface during the band maturity stage (0300–0600 UTC), when the radar and model analyses suggested conditions conducive to dendritic growth. Unfortunately, this event occurred prior to the dual-polarization upgrade; as discussed below, radar polarimetry provides substantially improved detection of such growth regions over use of Z_H alone.

b. 8–9 February 2013

The historic 8–9 February 2013 northeastern blizzard has been studied extensively (Griffin et al. 2014; Picca et al. 2014; Ganetis and Colle 2015), and produced some of the most extreme winter storm polarimetric radar signatures thus far observed (Griffin et al. 2014). This includes vigorous planar crystal growth regions called dendritic growth zones (DGZs) in the literature, which polarimetric radars can detect as enhancements of specific differential phase K_{DP} and/or differential reflectivity Z_{DR} near −15°C (Kennedy and Rutledge 2011; Andrić et al. 2013; Bechini et al. 2013; Schneebeli et al. 2013; Schrom et al. 2015).

At 1500 UTC 8 February 2013, WPC analyzed an inland coastal front over Connecticut and eastern Massachusetts. At the same time, the incipient 992-hPa surface low was located off the coast of Virginia Beach, Virginia. Over the next 9 h, the low rapidly intensified, occluded, and moved northeastward, located south of Cape Cod and southeast of Long Island by 0000 UTC with an analyzed minimum pressure of 979 hPa. This placed Long Island in an intense mesoscale precipitation band located within the comma-head region of the cyclone (Fig. 3b). Throughout the analysis period, surface winds at Islip Airport gradually backed from northeasterly to northwesterly as temperatures gradually dropped (Fig. 2b). These measurements (and WPC surface analyses) show no frontal passages throughout the event.

Time–height QVP plots of this storm reveal the extreme nature of this event, with larger low-level Z_H (>50 dBZ) and larger Φ_{DP} accumulations (>30° at 10° elevation angle) than any other case shown herein (Figs. 5a,b). The large Φ_{DP} accumulation between

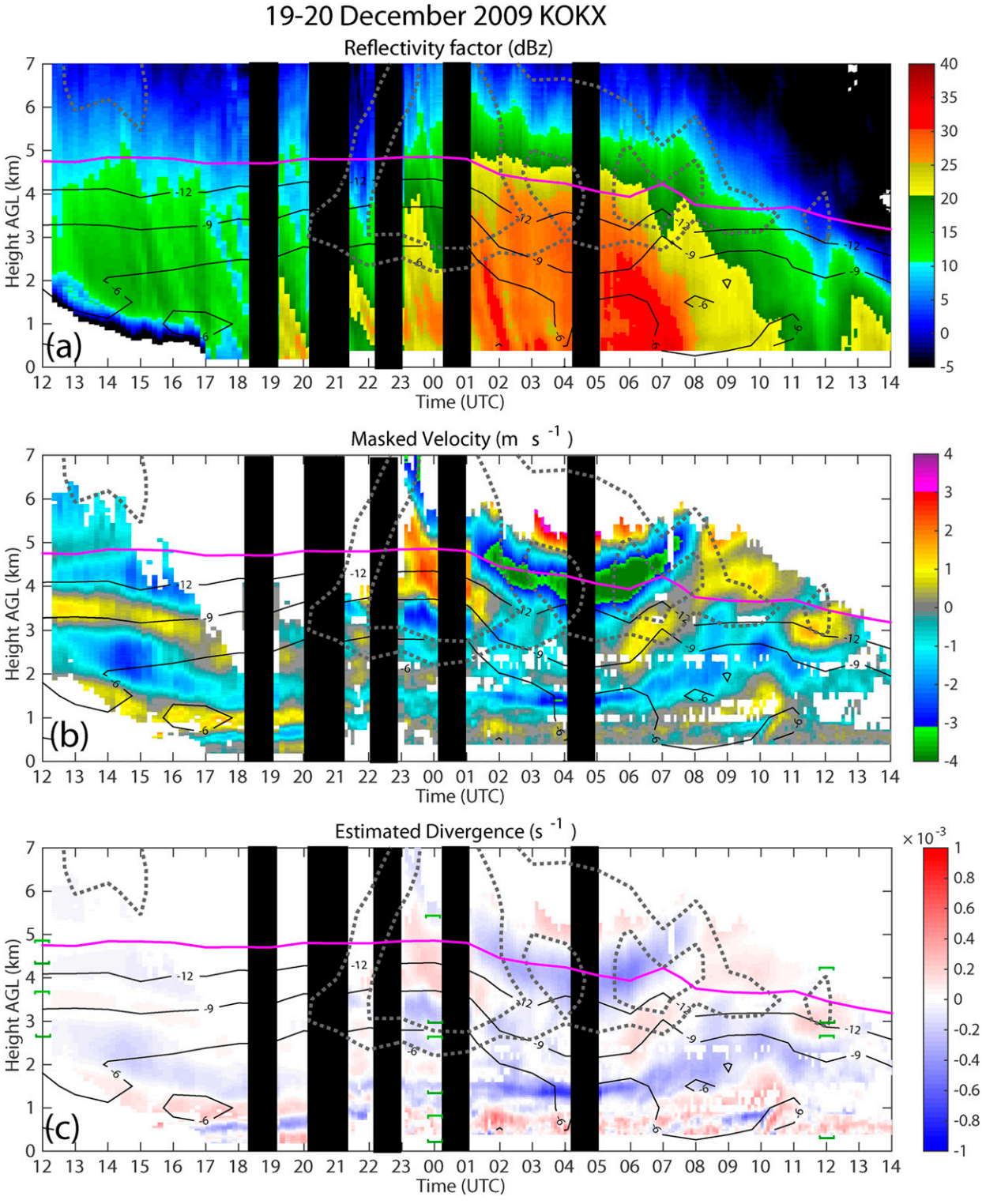

FIG. 4. Time–height QVPs of (a) Z_H, (b) V_R, and (c) $\bar{\delta}$ from 19 to 20 Dec 2009. Vertical bars indicate missing data. Contours of RAP-analyzed temperature starting at −15°C (magenta) in 3°C increments (black) and ω starting at $-1\ \mathrm{Pa\,s^{-1}}$ in $-1\ \mathrm{Pa\,s^{-1}}$ increments (heavy dotted) are overlaid. Green brackets at 0000 and 1200 UTC correspond to layers of significant veering winds observed in operational soundings.

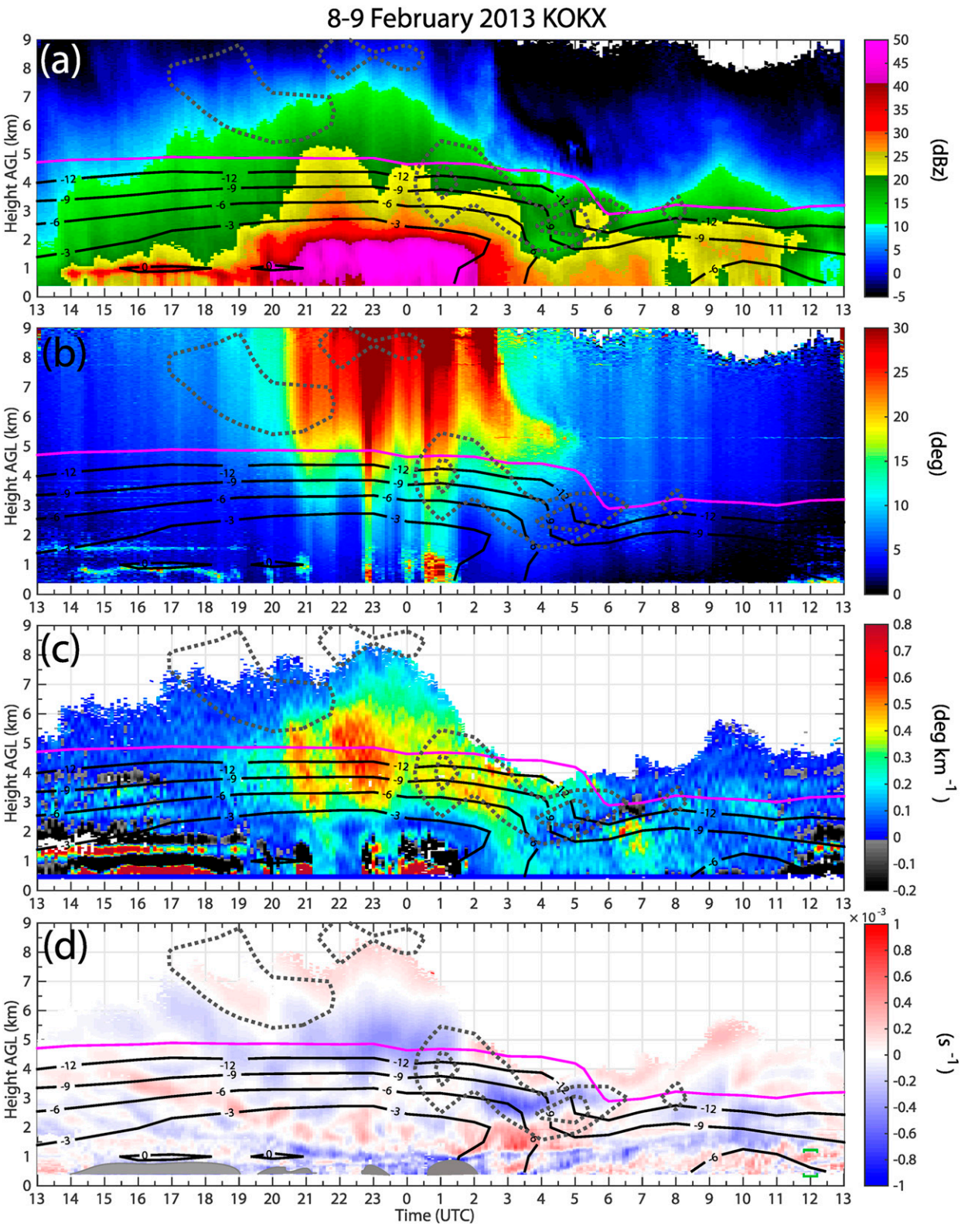

FIG. 5. Time–height QVPs of (a) Z_H, (b) Φ_{DP}, (c) K_{DP}, and (d) $\overline{\delta}$ from the 8–9 Feb 2013 blizzard. Overlaid are the −15°C (magenta) and 0° to −12°C contours (black) in 3°C increments, as well as RAP-analyzed vertical motion (gray/dark heavy dotted curves) as before. Note the expanded ranges in the color scales compared to other plots. In (d), gray shading censors regions of rain where the fall speed assumption is violated. Green brackets at 1200 UTC correspond to a layer of significant veering winds observed in the operational sounding.

2100 UTC 8 February and 0300 UTC 9 February (Fig. 5b) encompasses the RAP-analyzed −15°C contour, corresponding to averaged K_{DP} values >0.6° km^{-1} (Fig. 5c). In contrast, Z_{DR} magnitudes (not shown) are <1 dB, highlighting the different levels of informative content of these variables. These nuances are detailed in section 4. Such extreme K_{DP} signatures are thought to signify large concentrations of pristine planar crystals (possibly dendrites), implying highly efficient aggregation (Schrom et al. 2015; Moisseev et al. 2015). This is coincident with strong ascent implied by the $\overline{\delta}$ field (Fig. 5d). The RAP-analyzed vertical velocity fields seemingly do not agree with the radar-inferred ascent or enhanced snowfall, suggesting model error. Recall that the RAP data are from prior to the upgrade. Unfortunately, the 0000 UTC sounding is unavailable for comparison with the observed ascent.

Picca et al. (2014) report large SLRs (13:1) and snowfall rates (4.0–8.5 cm h^{-1}) near the KOKX radar site after the onset of this DGZ, from 2115 to 2245 UTC. During this time, 2–4-cm aggregates were reported, with dendrites and plates as the dominant habits observed at the surface at Stony Brook University in Stony Brook, New York (Ganetis and Colle 2015). This suggests a relationship between DGZs (large Φ_{DP} accumulations local or K_{DP} maxima near −15°C) and efficient aggregation leading to large SLRs (>10:1). Such a correlation was also found in snowstorms in Finland (D. Moisseev 2015, personal communication).

Though the extreme DGZ and implied vertical motion persists (and actually intensifies) beyond this time, the low-level thermodynamic structure changed markedly after 2245 UTC (Picca et al. 2014). This resulted in dramatically reduced SLRs (4:1 to 8:1) and heavy riming, sleet, and even irregular wet-growth-like ice hydrometeors termed ''asteroid ice'' from about 2330 to 0230 UTC (Griffin et al. 2014; Picca et al. 2014; Ganetis and Colle 2015). During this period, the QVPs reveal large (>50 dBZ) Z_H and large Φ_{DP} (implying contributions from backscatter differential phase) at low levels (Figs. 5a,b) coincident with reduced ρ_{hv} (not shown), possibly indicating electromagnetically large hydrometeors like asteroid ice undergoing wet growth, as suggested by Griffin et al. (2014) and Picca et al. (2014), leading to resonance scattering effects.

From 0230 to 0345 UTC, SLRs increased again to 8:1 to 10:1, with average snowfall rates near 6.6 cm h^{-1} (Picca et al. 2014). Ganetis and Colle (2015) report a mixture of crystal habits at these times, including plates, needles, and columns. The QVP shows a general decrease in Z_H, Φ_{DP}, and K_{DP} through this period (Figs. 5a–c). Interestingly, at about 0200 UTC the $\overline{\delta}$ QVP (Fig. 5d) shows a sudden ~2-km decrease in the altitude of the implied ascent, to a temperature range from −6° to −12°C. The RAP-analyzed ascent also descends about 2 km around this time. This temperature range encompasses the transition from columnar to platelike habits (at −8°C). Enhanced K_{DP} values indicating large concentrations of nonspherical crystals extend to the surface; collectively, these radar observations are consistent with the range of habits at the surface reported in Ganetis and Colle (2015) during this period. A strong divergence signature (implying descent) below 2 km after 0200 UTC may be associated with cold-air advection and large-scale descent behind the low. Indeed, temperatures at Islip Airport decreased throughout this period (Fig. 2b), and the 1200 UTC sounding (not shown) reveals backing winds in this layer. The simulations by Ganetis and Colle (2015) also suggest that cold-air advection contributed to cooling and stabilization of this layer.

Between 0500 and 0600 UTC, the RAP-analyzed −15°C contour drops by over 1 km in altitude such that it is closer to the level of radar-inferred ascent. This coincides with a sudden changeover in surface crystal habits to predominantly dendritic crystals (Ganetis and Colle 2015). Also during this period, the magnitude of radar-inferred ascent is decreasing. Though an increase in Φ_{DP} is still evident, particularly between 0600 and 0800 UTC, it is much smaller in magnitude, in accord with the reduction in the inferred ascent magnitudes.

c. 15–16 February 2014

WPC surface analyses indicate the storm began as a 998-hPa low over Elizabeth City, North Carolina, at 1500 UTC on 15 February 2014. It deepened by 30 hPa over the proceeding 24 h and, thus, can be classified as a ''bomb'' (e.g., Sanders and Gyakum 1980); the majority of this intensification (19 hPa) occurred between 2100 UTC 15 February and 0600 UTC 16 February. By 0300 UTC, the center of the low was southeast of Cape Cod. It rapidly made its way northeastward, reaching Nova Scotia by 1500 UTC 16 February. A mesoscale snowband developed between 2200 and 2300 UTC over southeastern Massachusetts (Fig. 3c), in the comma head of the deepening cyclone, but then quickly pushed eastward off the coast of Cape Cod just before 0500 UTC 16 February. WPC surface analyses do not indicate any frontal passages during the event; Boston airport ASOS data are consistent with these analyses, showing temperatures holding steady just below 0°C throughout much of the event as winds gently backed from northeasterly to north-northwesterly (Fig. 2c).

KBOX observations of the 15–16 February storm reveal a rather uniform structure for nearly 12 h (Fig. 6).

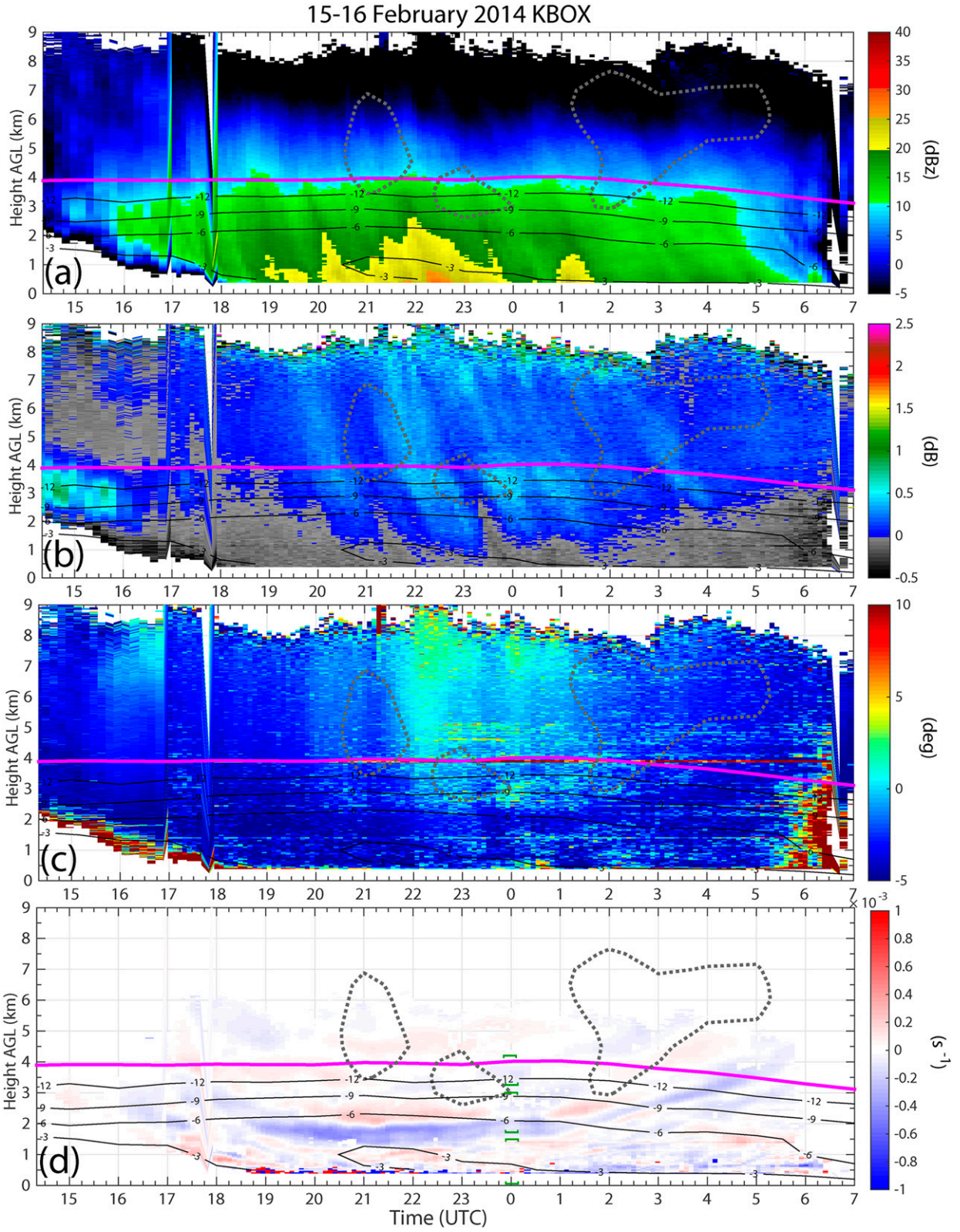

FIG. 6. Time–height QVPs of (a) Z_H, (b) Z_{DR}, (c) Φ_{DP}, and (d) $\overline{\delta}$ from 15 to 16 Feb 2014, taken by KBOX at 10° elevation. Contours and brackets overlaid as in Fig. 4.

Interestingly, though the Z_H gradient near −15°C is persistent, only occasional slight Z_{DR} and Φ_{DP} enhancements are visible (Figs. 6b,c), demonstrating a stark contrast with the previous case's spectacular DGZ. Estimated K_{DP} values are $<0.05^\circ\,km^{-1}$ (not shown). The small polarimetric contrasts suggest that particles dominating the overall Z_H are not very oblate, and that any oblate particles present are small and/or in low concentrations. The Z_{DR} and Φ_{DP} enhancements are most noticeable between 2000 and 0200 UTC, when weak implied and analyzed ascent straddles the −15°C level. Surface precipitation rates are maximized during this time: ASOS measurements from BOS indicate hourly liquid-equivalent precipitation accumulations between 0.75 and 1.5 mm, which is 2–3 times greater than at other times during this event. Rising motion near −15°C could promote growth toward planar habits of activated ice nuclei and/or the smallest crystals falling from above (e.g., Sulia and Harrington 2011). Otherwise, larger, compact particles falling from above will not obtain extreme aspect ratios. Clearly, though, the planar or dendritic growth lacks the vigor observed in the 8–9 February 2013 case.

Between about 1900 and 0000 UTC, the low-level Z_H is enhanced below 2 km AGL, with maximum values >20 dBZ (Fig. 6a). This is coincident with a band of inferred ascent centered at about 2 km AGL (Fig. 6d). Although the KCHH sounding is taken ~103 km downstream of KBOX, the two veering layers aloft identified at 0000 UTC show some consistency with the radar-inferred ascent regions. This ascent corresponds to temperatures >−6°C. Primary ice nucleation is unlikely in such warm conditions, so one may expect supercooled liquid droplet activation. The Z_H enhancement and Z_{DR} decrease at this level are consistent with snow growth by riming, as particles increase in effective density and their aspect ratios become closer to unity (e.g., Kumjian et al. 2014; Vogel et al. 2015; Kumjian et al. 2016). Unfortunately, surface observations are not available during this event to validate the radar-based inferences.

d. 24–25 January 2015

In some ways, the 24–25 January 2015 event (Fig. 3d) was unmemorable given the intense storm that occurred shortly afterward (see the next subsection). Nonetheless, the WSR-88D data reveal several noteworthy features. According to WPC surface analyses, the storm began as a 999-hPa low over Elizabeth City at 0900 UTC 24 January. The low deepened rapidly (40 hPa in 24 h, attaining bomb status) as it moved quickly up the coast. By 0300 UTC 25 January, it was centered over Nova Scotia. No analyzed fronts passed either BOS or ISP, but winds turned from southwesterly to northerly as the low approached and rapidly deepened while temperatures held steady at both locations (Fig. 2d). Though the low passed just southeast of Cape Cod, at 2100 UTC 24 January, infrared satellite imagery (not shown) suggests the storm failed to produce a robust comma-head cloud structure. Much of the precipitation from this event occurred earlier, associated with the "warm conveyor belt" (e.g., Browning 1971; Carlson 1980) ahead of the cyclone's advancing warm front.

According to the KBOX Z_H QVP (Fig. 7a), most of the heaviest precipitation fell between about 0900 and 1600 UTC 24 January. Throughout the duration of the event, Z_{DR} is consistently enhanced at the RAP-analyzed −15°C contour (Fig. 7b), indicating planar crystals. A prominent Φ_{DP} enhancement (Fig. 7c) is centered on about 1000 UTC, atop the tallest Z_H echoes. Additionally, this DGZ is collocated with radar-inferred and RAP-analyzed ascent (Fig. 7d), though the latter appears to maximize a bit early. (Note that the RAP analyses are from after the upgrade.) The correspondence of ascent near −15°C and heavier snowfall at the surface is in accordance with Auer and White (1982). This region of rising motion descends over the next several hours in both the RAP analyses and radar retrievals, although the RAP analysis places it about ~500 m above where the radar indicates it. Sounding-observed veering at 1200 UTC corresponds rather well to the radar-inferred ascent regions.

Between about 1200 and 1500 UTC, a melting-layer bright band appears in the Z_H, Z_{DR}, and Φ_{DP} QVPs (Figs. 7a–c) and ρ_{hv} (not shown), implying low-level warming and a changeover in surface precipitation type. Beneath, the presence of rain biases the $\overline{\delta}$ estimates (which are censored in the image). The RAP analyses at this location do not have any >0°C temperatures throughout this period. This demonstrates the value added by polarimetric radar data in identifying precipitation transitions, as well as model error. Griffin et al. (2014) report a similar situation in the 8–9 February 2013 case wherein the radar observations clearly show hydrometeor melting that is not supported by the RAP analyses.

Of note is a localized minimum in Z_{DR} collocated with enhanced Z_H just above the melting layer between 1300 and 1330 UTC. A subtle enhancement in the $\overline{\delta}$ field is also evident, centered at approximately 1300 UTC and 1.5 km AGL, possibly indicating slightly enhanced vertical motion. Interestingly, Φ_{DP} increases just above this pocket of negative Z_{DR}. The estimated K_{DP} during this time (not shown) suggests a maximum of 0.1°–$0.2^\circ\,km^{-1}$ between 2 and 3 km AGL, which corresponds to RAP temperatures of −3° to −6°C. This anticorrelation

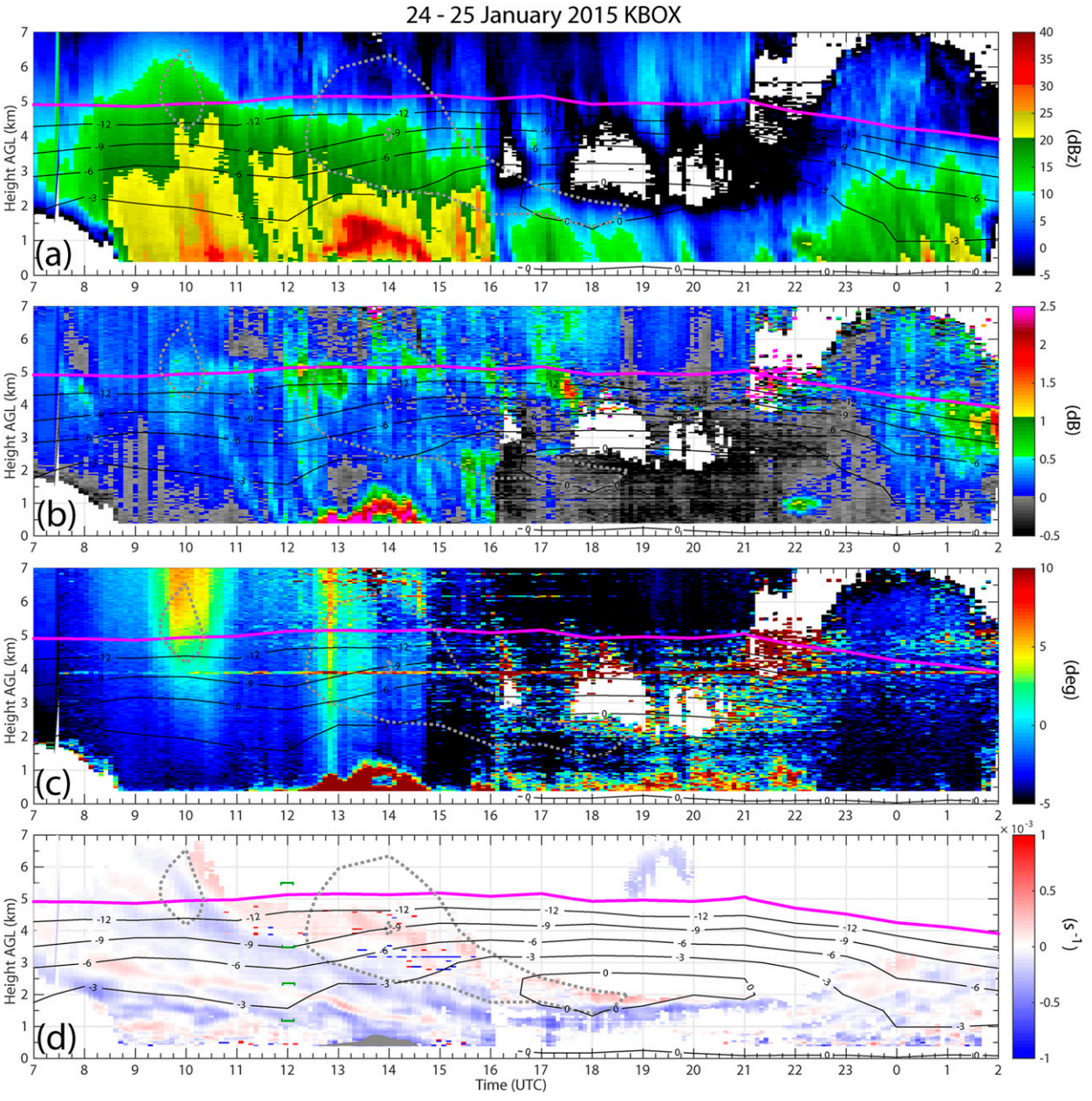

FIG. 7. Time–height QVPs of (a) Z_H, (b) Z_{DR}, (c) Φ_{DP}, and (d) $\overline{\delta}$ from 24 to 25 Jan 2015, taken by KBOX at 10° elevation. In (d), gray shading censors regions of rain where the fall speed assumption is violated. Contours and brackets overlaid as in previous figures.

between K_{DP} and Z_{DR} implies a mixture of particle habits: reduced Z_{DR} (possibly even to negative values) could mean more isotropic (and possibly vertically aligned) particles such as graupel, whereas the increasing Φ_{DP} (positive K_{DP}) clearly indicates oblate ice crystals. Taken together with the RAP-analyzed temperatures, we speculate that these signatures suggest ongoing riming and perhaps secondary ice production (e.g., Hallett and Mossop 1974), leading to needlelike crystals in conditions in which growth by vapor deposition would be favorable. Using in situ aircraft data, Kumjian et al. (2016) confirm the presence of a large concentration of needles at −4°C in a similar K_{DP} signature thought to be associated with secondary ice production.

From 1600 to 2200 UTC, the deeper echoes cease and give way to shallow (<2 km) echoes topped with a band of radar-inferred ascent. The RAP-analyzed $-1\,\mathrm{Pa\,s^{-1}}$ contour extends for the first 3 h of this period as well. The rising motion is located within RAP-analyzed

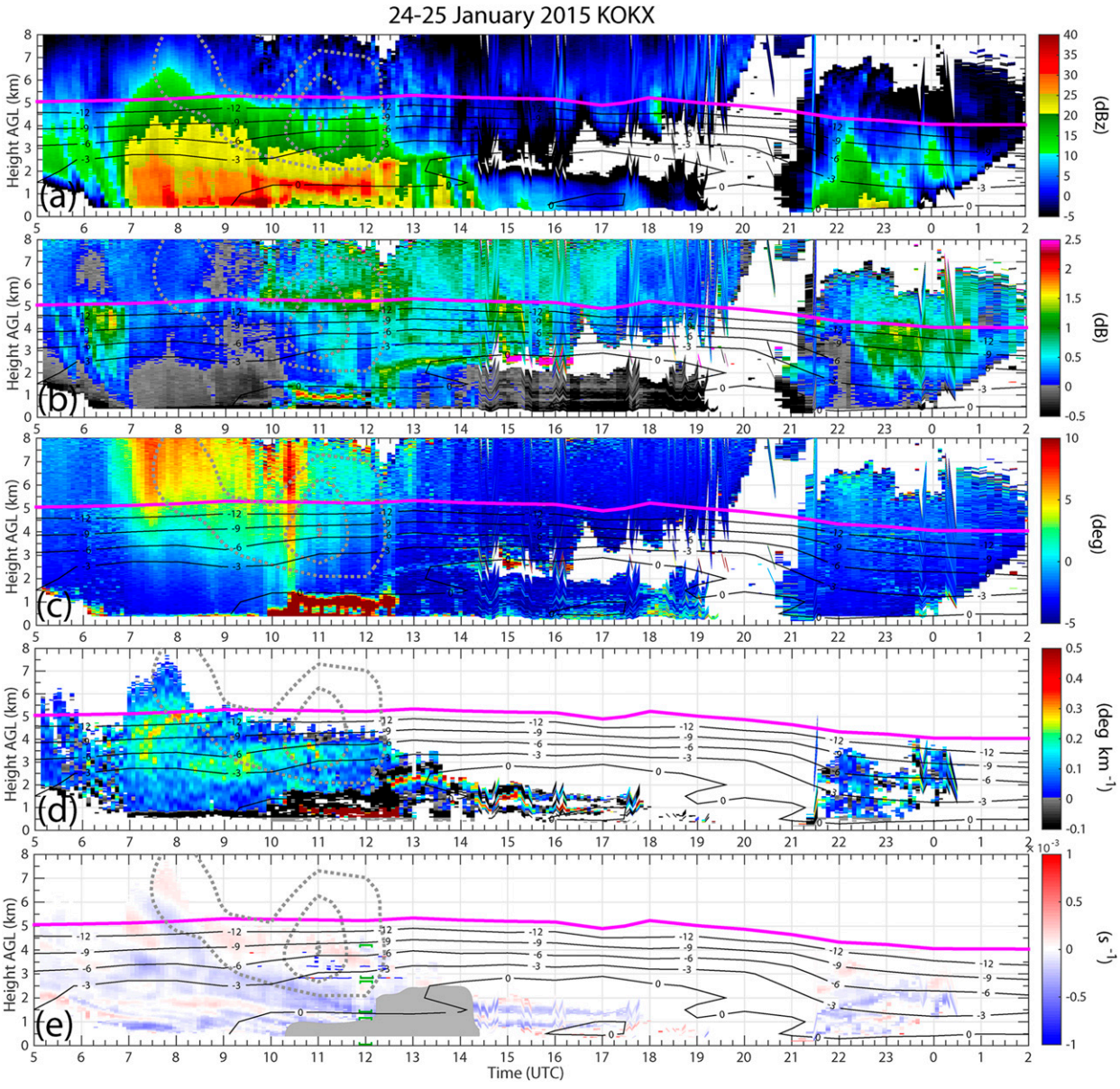

FIG. 8. Time–height QVPs of (a) Z_H, (b) Z_{DR}, (c) Φ_{DP}, (d) K_{DP}, and (e) $\overline{\delta}$ from 24 to 25 Jan 2015, taken by KOKX at 10° elevation. In (e), gray shading censors regions of rain where the fall speed assumption is violated. Contours and brackets overlaid as in previous figures.

temperatures >-3°C, which is too warm for primary ice nucleation. Thus, one is led to infer that so-called warm processes producing rain and drizzle are occurring. Indeed, METAR reports from Logan International Airport indicate rain and drizzle through this period with surface temperatures between 0° and 1°C. Public mPING reports also confirm rain and drizzle at the surface throughout this period (not shown). The widespread negative Z_{DR} is a result of a low bias.

The same case as viewed by KOKX (Fig. 8) reveals similar features, including heavier precipitation early on (Fig. 8a), a persistent Z_{DR} enhancement near -15°C (Fig. 8b), a prominent Φ_{DP} enhancement (~0730 UTC; Figs. 8c,d) collocated with a region of ascent that decreases in altitude with time (Fig. 8e), and the appearance of a melting-layer bright band after 1000 UTC (Figs. 8a–c) along with rain biasing the $\overline{\delta}$ estimates beneath. This time, however, the RAP analyses suggest a deeper pool of >0°C air beginning at about 0900 UTC (an hour early) and persisting throughout the rest of the period. Notably, the changes in altitude of the observed melting layer between 1000 and 1100 UTC and 1200 and 1300 UTC are rather abrupt and initially are not consistent with the RAP analyses. Of the three veering

layers in the 1200 UTC KOKX sounding, the middle one (1.5–2.7 km AGL) corresponds well to the radar-inferred ascent region.

Between 0700 and 1000 UTC, increases in Φ_{DP} begin at ~2.5 km AGL (Fig. 8c), corresponding to temperatures between −3° and −6°C. This band of positive K_{DP} has estimated maximum values approaching 0.3° km^{-1} (Fig. 8d) and sits atop a noticeable reduction in Z_{DR} (Fig. 8b) and increase in Z_H (Fig. 8a). Again, given the likely temperatures analyzed by the RAP model, these features suggest possible riming and secondary ice production. These features evolve similarly to those observed by KBOX, except consistently offset by ~3 h. This implies that, on the scales resolved by QVPs, the storm remained quasi steady state over this period. This case also demonstrates the independent information available from QVPs of different radar variables—information that would be lost if the fields were distilled into a single product such as hydrometeor identification.

e. 26–28 January 2015

The 26–28 January 2015 blizzard (Fig. 3e) came on the heels of the 24–25 January 2015 storm, with media coverage calling it ''historic'' and the ''Blizzard of 2015.'' The storm produced a swath of large snow accumulations (30–90 cm) from Long Island to Maine, causing major travel disruptions, widespread power outages, and at least two fatalities (Otto 2015). Though NYC was spared the storm's heaviest impacts, shutting down the city's transit system led to an estimated $200 million in economic losses.

At 1800 UTC 26 January, the storm was a 998-hPa low off the coast of Virginia Beach. Over the next 18 h, the low moved northeastward and deepened rapidly, occluded, and stalled southeast of Cape Cod at 1200 UTC 27 January with a minimum pressure of 975 hPa. In contrast to the previous storm, the 26–28 January event featured a robust comma-head cloud pattern visible in infrared satellite imagery (not shown). After maintaining that intensity for the next several hours, it gradually began to weaken and continue slowly northeastward, reaching the southern coast of Nova Scotia by 1200 UTC 28 January. The winds at both ISP and BOS gradually back from northeasterly to northwesterly throughout the event (Fig. 2e); no analyzed frontal passages occurred during this event.

Intermittent snow began early in the day on 26 January at and around KOKX and became more persistent after 1700 UTC (Fig. 9). The $\overline{\delta}$ QVP (Fig. 9e) implies weak ascent between about 1.5 and 3 km AGL from 1800 to 2000 UTC, corresponding to about −5° to −11°C. The RAP analyses also suggest weak ascent at these levels, though about 1–2 h late. The upper two veering layers identified in the 0000 UTC sounding correspond well to radar-inferred regions of ascent. The Φ_{DP} QVP (Fig. 9c) reveals subtle but persistent increases through this layer, corresponding to K_{DP} values <0.1° km^{-1} over the next several hours (Fig. 9d).

Heavier snow (as inferred from larger low-level Z_H) began shortly after 0000 UTC 27 January, and was especially noticeable at 0200 UTC. At this time, larger increases in Φ_{DP} (Fig. 9c) are present near the −15°C level, coincident with implied ascent from $\overline{\delta}$ QVPs (Fig. 9e). The largest Φ_{DP} increase occurs between 0600 and 0700 UTC, corresponding to maximum K_{DP} values between 0.3° and 0.4° km^{-1} just below the −15°C level (Fig. 9d). Stronger ascent is also evident in the RAP results at this time, centered on the −15°C contour. Human-augmented METARs from ISP, ~21 km southwest of KOKX, confirm these inferences. ISP reported the heaviest snow (≥5 cm h^{-1}) between 0400 and 0900 UTC, with a peak of ~7.5 cm accumulating between 0700 and 0800 UTC (Fig. 10). Thus, radar QVPs, RAP hourly analyses, and surface accumulation reports are consistent in depicting the heaviest snowfall rates coinciding with the appearance of a robust DGZ associated with enhanced vertical motion near −15°C. The lack of a large Z_{DR} enhancement associated with the K_{DP} signature is consistent with one of the ''flavors'' of DGZs described in Schrom et al. (2015): the most robust K_{DP} signatures are associated with large crystal concentrations that lead to more efficient aggregation and thus higher Z_H and lower Z_{DR} (Schrom et al. 2015; Moisseev et al. 2015).

The same event was also observed at KBOX (Fig. 11). Both the RAP and radar suggest stronger ascent over KBOX than over KOKX, maximizing near 1000–1100 UTC, though the radar suggests strong convergence between 2 and 3 km AGL continuing for another few hours. The 1200 UTC KCHH sounding indicates a deep layer of veering from 0.6 to 4.3 km that corresponds well to the radar-inferred ascent, at least above the boundary layer. Coincident with this ascent maximum is a large enhancement in Φ_{DP} (larger than the KOKX case) around −15°C. Interestingly, there are three distinct Φ_{DP} enhancements: the largest between 1000 and 1100 UTC, with maximum K_{DP} values exceeding 0.4° km^{-1}, and two others centered near 0800 and 0500 UTC. Maximum K_{DP} values at 0500 UTC are <0.2° km^{-1}. The largest K_{DP} at 0800 UTC actually occurs at low levels, corresponding to temperatures >−9°C and suggesting columnar crystal growth, in contrast with the other two Φ_{DP} enhancements.

f. 5–6 March 2015

The 5–6 March 2015 case was not characterized by a well-defined coastal cyclone; nonetheless, parts of the

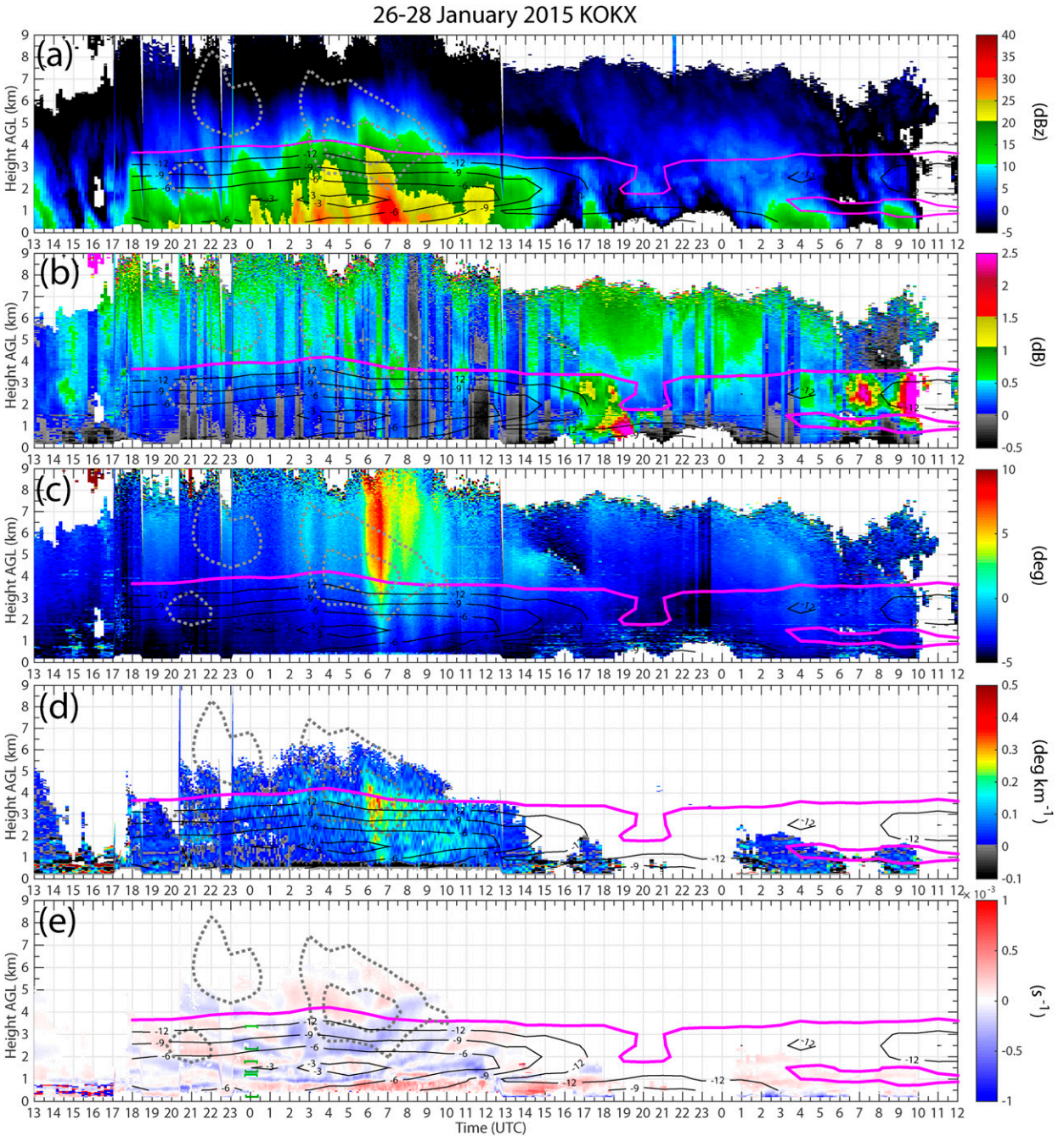

FIG. 9. Time–height QVPs of (a) Z_H, (b) Z_{DR}, (c) Φ_{DP}, (d) K_{DP}, and (e) $\overline{\delta}$ from 26 to 28 Jan 2015, taken by KOKX at 10° elevation. Contours and brackets overlaid as in previous figures. Streakiness in Z_{DR} appears to be a result of the Z_{DR} offset changing in time.

northeastern United States still received winter precipitation (Fig. 3f), including a precipitation transition across central Long Island and southern Connecticut. The NWS Forecast Office in Upton received ~18.5 cm of snow from the event, according to a public information statement from early on 6 March. Aloft, a high-amplitude positively tilted trough was present to the west, its axis moving across the central plains during the period of analysis. The northeastern United States generally was within the right-entrance region of a strong jet streak (peak winds >80 m s^{-1} at about 200 hPa in KOKX soundings). At the surface, an elongated region of low pressure was analyzed off the coast, and a diffuse cold front was pushing through the region. The

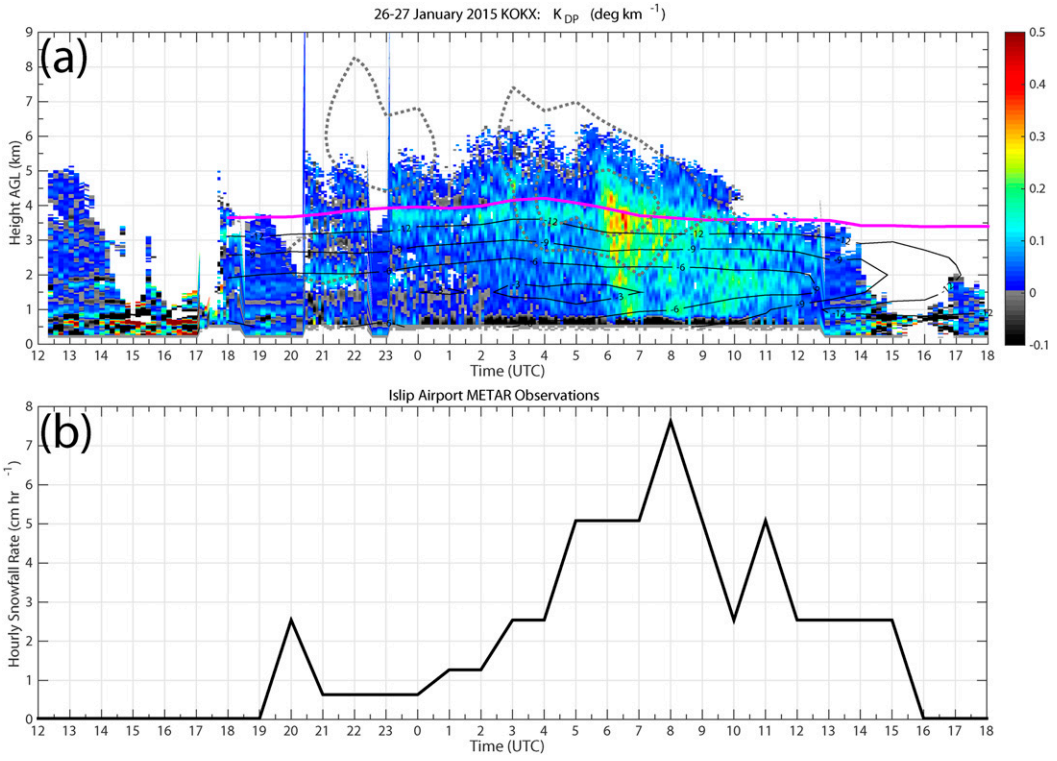

FIG. 10. (a) QVP of K_{DP} from 26 to 28 Jan 2015 taken by KOKX at 10° elevation; contours are as in previous figures. (b) Hourly snowfall rate (cm h^{-1}) based on METAR-reported snow accumulations over the preceding hour at KISP from 1200 UTC 26 Jan to 1800 UTC 27 Jan. Trace amounts are set to 0.0254 cm (0.01 in.).

cold front passed over central Long Island between 0900 and 1000 UTC, accompanied by a shift in winds from westerly to northerly, and decreasing temperatures (Fig. 2f).

RAP data for the case were unavailable for the first ~18 h of the event. Nonetheless, the radar data strongly suggest the −15°C level remained steady during this period, clearly discernable as a large vertical Z_H gradient (Fig. 12a) and enhancement in Z_{DR} (Fig. 12b) between about 5 and 6 km AGL, indicating rapid growth by aggregation and the presence of planar crystals, respectively. Indeed, observed KOKX soundings at 0000 and 1200 UTC 5 March indicate the −15°C levels were at ~5.9 and ~5.8 km AGL, respectively. Additionally, Φ_{DP} accumulations (Fig. 12c) and a slight reduction in ρ_{hv} (Fig. 12d) are evident at this level throughout the period. The ρ_{hv} reduction occurs where a large diversity of particle shapes exists, likely where very nonspherical planar crystals and more isometric crystals and/or aggregates contribute about equally to the overall backscattered signal (e.g., Doviak and Zrnić 1993; Andrić et al. 2013; Kumjian 2013a,b). After sufficient aggregation, larger, isotropically scattering aggregates dominate the backscattered signal, causing ρ_{hv} to increase in value toward unity as Z_{DR} decreases toward small positive values below about 4.5 km AGL.

The melting layer is quite visible in Z_H, Z_{DR}, Φ_{DP}, and ρ_{hv} between about 0200 and 1000 UTC (Figs. 12a–d), and in biased $\overline{\delta}$ owing to rain (Fig. 12e). The "blips" in Φ_{DP} at the melting layer indicate the backscatter differential phase owing to electromagnetically large hydrometeors, presumably large melting aggregates. At times (e.g., ~0800 UTC), backscatter differential phase values of nearly 15° are observed, whereas other times (e.g., ~0500–0600 UTC) display very little backscatter differential phase. Recent studies by Trömel et al. (2013, 2014) have also documented the backscatter differential phase in melting layers at S, C, and X bands. They suggest that the large range of observed values provides information about microphysical processes within and above the melting layer; namely, low values suggest compact or rimed particles falling into the melting layer, whereas large values indicate substantial aggregation within the melting layer. Because microphysical processes above and within the melting layer can affect the resulting drop size distribution beneath, long-term statistical analyses of these characteristics may prove useful for quantitative precipitation estimation.

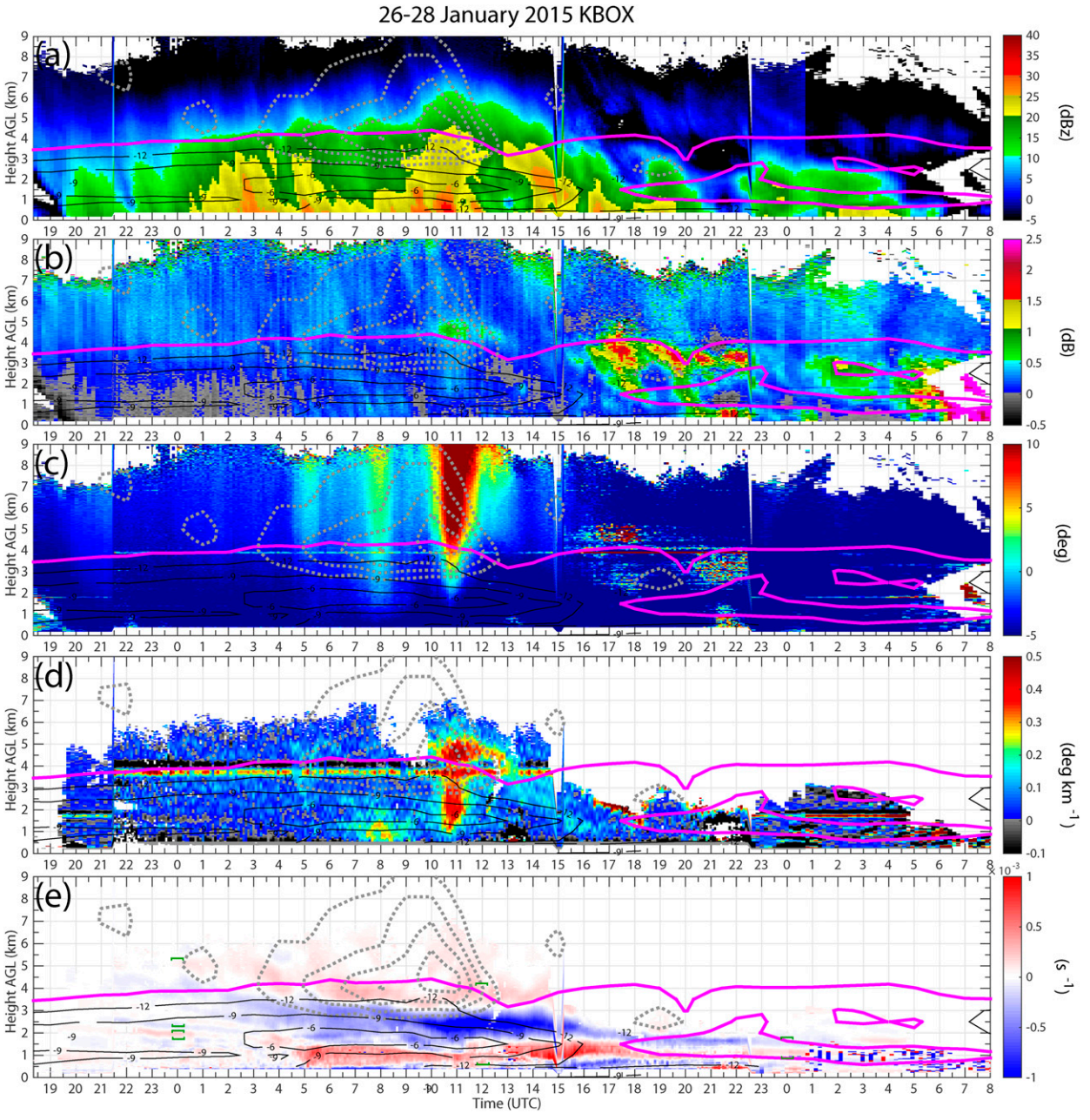

FIG. 11. Time–height QVPs of (a) Z_H, (b) Z_{DR}, (c) Φ_{DP}, (d) K_{DP}, and (e) $\overline{\delta}$ from 26 to 28 Jan 2015, taken by KBOX at 10° elevation. Contours and brackets are overlaid as in previous figures. The persistent K_{DP} dipole located near 4 km AGL is an artifact of ground clutter contamination owing to radar sidelobes.

As in other cases, we see the melting layer take rapid excursions in altitude. For example, the melting-layer height increases by nearly 1 km between 0430 and 0500 UTC, then suddenly drops in altitude, exhibits a double structure between 0900 and 1000 UTC, and disappears by 1000 UTC. This corresponds well to a changeover of mPING reports (Fig. 13) from mainly rain to snow across central Long Island between 0900 and 1000 UTC. Overlaid markers at the ASOS station in Fig. 13d indicate that different precipitation types were observed during the 30-min period. The changeover from rain to snow at the ASOS station occurred at 0949 UTC.

The $\overline{\delta}$ field (Fig. 12e) shows persistent convergence and implied ascent at about 5 km AGL from 0000 to 0900 UTC, followed by a region of implied ascent that slopes upward in time from 1000 to 2300 UTC.

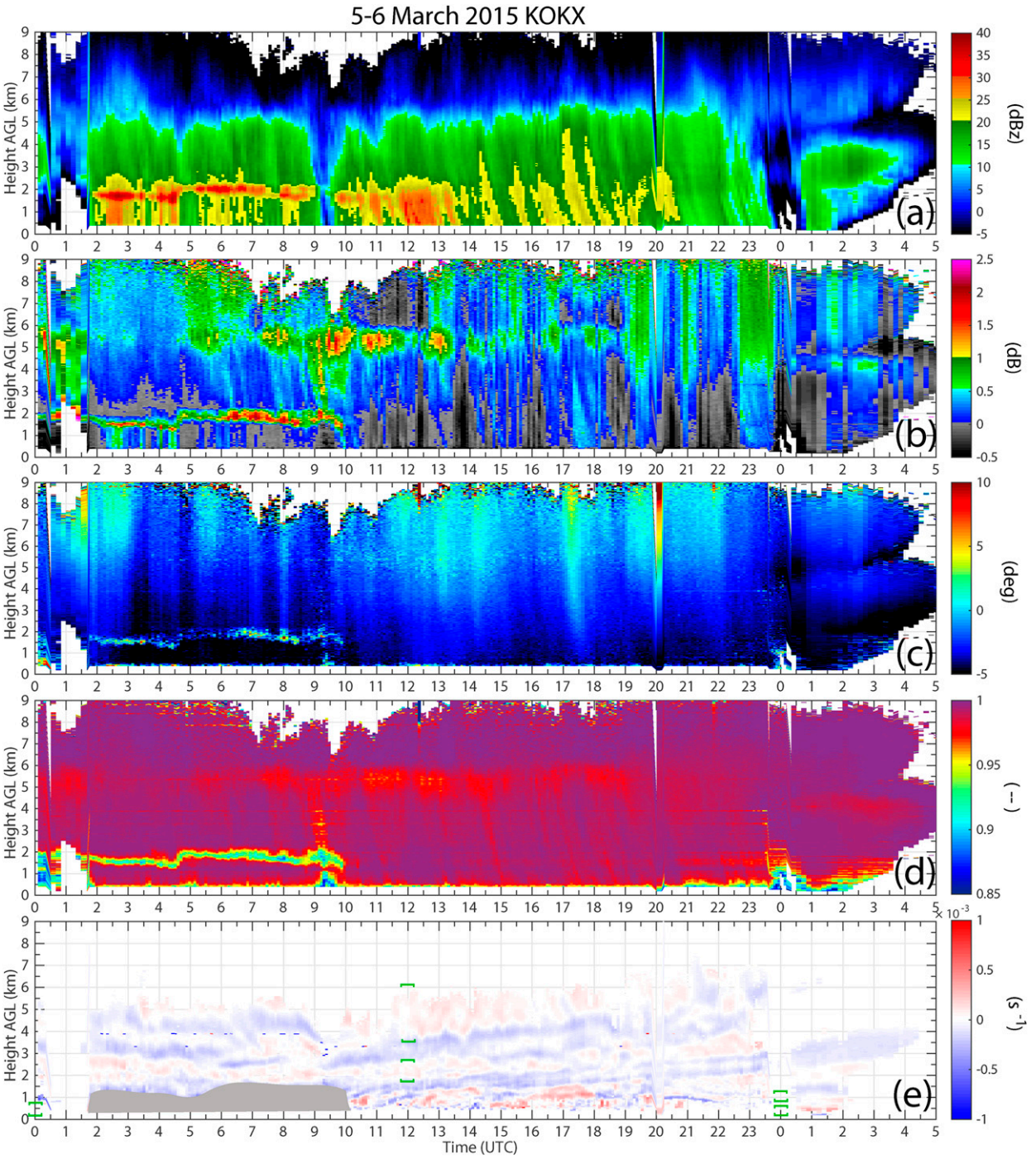

FIG. 12. Time–height QVPs of (a) Z_H, (b) Z_{DR}, (c) Φ_{DP}, (d) ρ_{hv}, and (e) $\overline{\delta}$ from 5 to 6 Mar 2015, taken by KOKX at 10° elevation. In (e), gray shading censors regions of rain where the fall speed assumption is violated. Brackets are overlaid as in previous figures.

Interestingly, the break in the $\overline{\delta}$ patterns coincides with the sudden downward excursion of the melting layer (most evident in Z_{DR} and ρ_{hv}) and the changeover in surface precipitation associated with a cold frontal passage. After 1000 UTC, the low-level Z_H shows enhancements similar to a bright band, despite the lack of melting signatures in the polarimetric variables. The 1200 UTC soundings from KCHH and KOKX reveal isothermal layers near 0°C below about 2 km AGL (not shown), coincident with the enhanced Z_H values

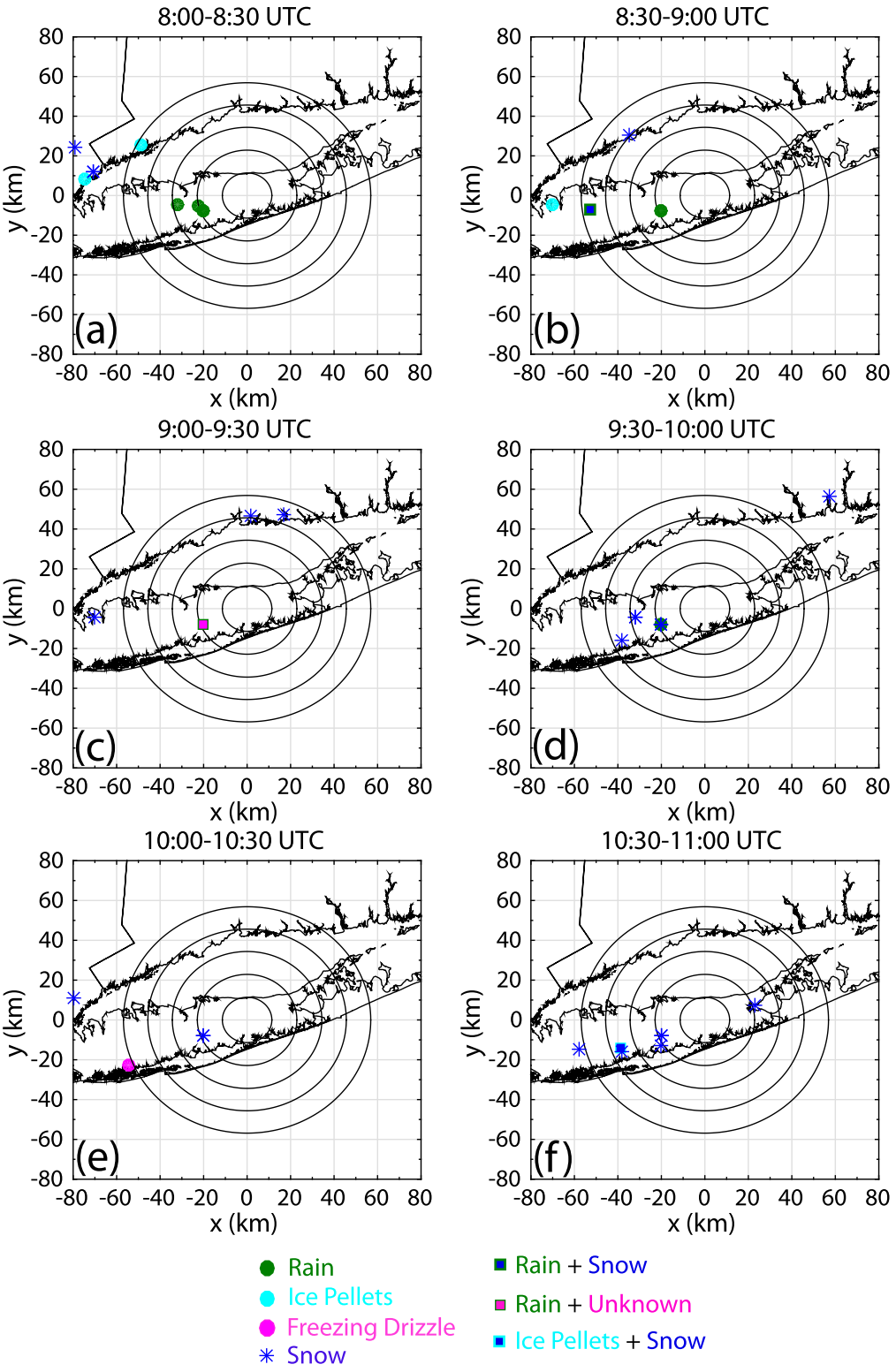

FIG. 13. The mPING and ASOS precipitation reports at (a) 0800–0830, (b) 0830–0900, (c) 0900–0930, (d) 0930–1000, (e) 1000–1030, and (f) 1030–1100 UTC 5 Mar 2015. Precipitation types shown are rain (green circles), ice pellets (cyan circles), snow (blue asterisks), and freezing drizzle (magenta circles). Mixtures of precipitation types are shown in squares: rain and snow, green trim and blue fill; rain mixed with "unknown precipitation," green trim and magenta fill; and ice pellets mixed with snow, cyan trim and blue fill.

observed in the QVP. This suggests efficient aggregation of snow falling through the comparatively warm layer from about 1000 to 1300 UTC. The KOKX 1200 UTC sounding also shows two veering layers that encompass the two radar-inferred ascent regions, albeit shifted toward the divergence portion of the signature (Fig. 12e).

In contrast to the sudden low-level changes, the planar crystal growth signatures between 5 and 6 km AGL remain steady throughout the period encompassing the frontal passage and low-level cold-air advection. This suggests the decoupled evolution of low- and upper-level thermodynamic structures, as well as a complex relationship between the kinematic and thermodynamic features throughout the storm's lifetime.

4. Discussion and conclusions

Polarimetric WSR-88D data collected during six northeastern U.S. coastal winter storms are analyzed. The data are presented in time–height plots of quasi-vertical profiles of the polarimetric Doppler radar variables, which reduces noise, facilitates comparisons with mesoscale NWP models, and provides information about bulk (averaged) microphysical and kinematic structures. Such QVPs add value over previous binning techniques and compare favorably to vertically pointing radar observations (e.g., Stark et al. 2013). Novel retrievals using QVPs of Doppler velocity reveal regions of implied mesoscale ascent over the radar site. Thus, for the first time, winter storm kinematic information (e.g., mesoscale ascent) is directly tied to microphysical information (e.g., polarimetric signatures) using dual-polarization WSR-88D observations.

An important signature repeatedly observed in our study is enhancements of Φ_{DP} (K_{DP}) and/or Z_{DR} near −15°C. Though these have been interchangeably referred to as DGZs in the literature, they likely have different microphysical interpretations. Kennedy and Rutledge (2011) were the first to analyze the signature at S band in detail, attributing it to dendritic growth and showing how precipitation intensity increased beneath it. They found Z_{DR} enhancements located above the K_{DP} enhancements, but did not provide an explanation. Further, their scattering calculations were unable to explain both Z_{DR} and K_{DP} enhancement magnitudes. Subsequent studies using S-, C-, and X-band radars (Andrić et al. 2013; Schneebeli et al. 2013; Bechini et al. 2013) also attributed both Z_{DR} and K_{DP} enhancements to dendritic growth, found the two enhancements to occur at different times and/or heights, and suggested the vertical profiles of radar variables beneath implied aggregation. Using a microphysical model, Andrić et al. (2013) were unable to reproduce the signature in all S-band polarimetric variables. They could only reproduce observed K_{DP} values by artificially enhancing the concentration of small, oblate ice crystals over that predicted by the model and thus concluded that some sort of ice multiplication process (not accounted for in the model) may explain the observations.

None of these studies was able to comprehensively explain the signature in all polarimetric radar variables using microphysical models and/or scattering calculations. This motivated Schrom et al. (2015) to analyze multiple cases in Colorado winter storms, in which they found large variability of the Z_{DR} and K_{DP} signatures at X band. Shallow stratiform cases produced pronounced Z_{DR} near echo top with lower Z_H and negligible K_{DP}, whereas cases with large K_{DP} also had large Z_H and the lowest Z_{DR}, implying ongoing aggregation. In these cases, K_{DP} maxima tended to be below echo top, suggesting particles falling into the layer from above. Using these observations and more sophisticated scattering calculations than previous studies, the authors retrieved realistic particle size distributions of plates and dendrites mixed with aggregates that quantitatively matched Z_H, Z_{DR}, and K_{DP} for each case.

Moisseev et al. (2015) examined C-band polarimetric radar data and advocates that the K_{DP} enhancement near −15°C is suggestive of "the onset of aggregation, rather than an indicator of a dendritic growth zone." They concluded that both aggregation and K_{DP} enhancements require large crystal populations (greater than those expected from primary nucleation) resulting from either a seeder–feeder mechanism or ice multiplication, consistent with the findings of Andrić et al. (2013). Using combined X-band vertically pointing Doppler and scanning polarimetric radar data, Schrom and Kumjian (2016) explained a persistent mean Doppler velocity minimum near −15°C in terms of populations of particles falling into the crystal growth layer and undergoing differential growth, similar to the seeder–feeder mechanism proposed by Moisseev et al. (2015). Schrom and Kumjian (2016) performed simple calculations that suggested this model is plausible for the cases they studied, and could explain bimodal Doppler spectra observed in previous studies (e.g., Moisseev et al. 2009; Zawadzki 2013).

Moisseev et al. (2015) also argue that early aggregates of planar crystals are oblate dense particles that could contribute to the K_{DP} enhancement. This assumes such aggregates comprise crystals sticking together in such a way that always leads to oblateness and stable orientations, which seems unlikely given the somewhat random nature of ice–ice collisions. The more sophisticated scattering calculations performed in Schrom et al. (2015)

suggest that larger dendrites (and, by extension, early aggregates) do not contribute as much as smaller crystals to K_{DP} if particle size distributions resemble traditional exponential or gamma functions. Further, K_{DP} enhancements at temperatures favoring columnar crystal growth in our present study (e.g., the 24–25 January 2015 case) and Kumjian et al. (2016), including aircraft observations of large numbers of needles in the latter study, point to high concentrations of pristine crystals as a more likely explanation for the enhanced K_{DP} values.

In an attempt to explain the differences between the Z_{DR} and K_{DP} signatures, some studies (e.g., Andrić et al. 2013; Thompson et al. 2014) have assumed dendrites have lower effective densities and thus Z_{DR} values than higher-density platelike crystals[3] owing to their branched structure and hollowing resulting from high-supersaturation growth (e.g., Nelson and Knight 1998). However, Oue et al. (2016) observed X-band $Z_{DR} > 7$ dB in sparse populations of large pristine dendrites in the Arctic; the extreme aspect ratios presumably dominated the reduction in effective density. (The low particle concentrations made K_{DP} estimates unreliable in that study.) The scattering calculations by Schrom et al. (2015) also suggest high Z_{DR} values are possible for both plates and dendrites. Therefore, *it may be difficult to discern whether true dendritic growth is occurring versus planar crystal growth without complementary observations* (e.g., saturation levels and/or in situ particle imagery).

Building on this body of work, our present study has added several insights into these signatures. We have demonstrated that larger radar-inferred ascent at −15°C corresponds to larger K_{DP} values. This suggests K_{DP} enhancements are more common in environments with greater supersaturations. Heavy snow identified in QVPs as enhanced Z_H near the surface most often occurred beneath such rising motion at −15°C and the associated increases in Φ_{DP}. This is in agreement with the suggestions of Auer and White (1982), but demonstrated herein with a single instrument (WSR-88D). At the surface, such instances of fluffy aggregates of dendritic crystals were characterized by large snow-to-liquid ratios (SLRs) and snowfall rates, in the limited number of cases in which those data were available. More complete observations of snowfall rates and SLRs are needed to verify this relationship; however, these observations do support the notion that enhanced K_{DP} observed near −15°C suggests heavier snowfall beneath, which may be valuable information for forecasters when viewing regions far from the radar where low levels are not adequately sampled. Additionally, Z_{DR} enhancements in the absence of enhanced K_{DP} still are associated with aggregation fingerprints in Z_H, albeit not as robust. This implies that aggregation is efficient at −15°C, perhaps irrespective of whether or not dendrites are present. We speculate this may be related to maximized depositional growth rates at this temperature (e.g., Takahashi et al. 1991) that lead to differential growth and fall speeds, increasing the probability of ice–ice collisions.

Synthesizing our results with those of prior studies, we conclude that the Z_{DR} enhancement should be more common than the K_{DP} enhancement if indeed increased Z_{DR} simply marks the beginning of planar crystal growth. Only in cases of sufficiently high number concentrations of planar crystals should K_{DP} be enhanced (e.g., seeder–feeder, ice multiplication, larger supply of ice nuclei, etc.). Larger supersaturations achieved by greater ascent magnitudes could increase the likelihood of K_{DP} enhancements by being conducive for rapid depositional growth (broadening the size spectrum, which would also promote aggregation) and/or nucleation of new crystals. This leads to heavier snow beneath associated with larger SLRs (>10:1).

In addition to the −15°C signatures, some cases exhibited Φ_{DP} enhancements at higher temperatures. These could be from fallout of dendrites not aggregated, or columnar crystals produced locally at higher temperatures (>−8°C), possibly related to secondary production and riming. This was observed in both KOKX and KBOX data from 24 to 25 January (Figs. 7 and 8) and is consistent with other studies indicating secondary ice production (Kumjian et al. 2016). QVPs can reveal such small K_{DP} values that may not otherwise be observable using traditional data interrogation techniques like PPI scans in which random noise makes K_{DP} estimation difficult. We speculate that high-frequency radar observations may reveal more prominent examples of such Φ_{DP} enhancements associated with nonspherical crystals. Aircraft in situ data are needed to determine habit types associated with these polarimetric signatures. This study also showed abrupt transitions in precipitation type at low levels inferred from sudden excursions of the melting layer. Surface precipitation-type transitions revealed in mPING observations confirm these radar-based inferences (e.g., the 5–6 March

[3] A more correct physical explanation involves thinking of crystals as comprising a large number of small dipole oscillators (e.g., Bohren and Huffman 1983). Owing to gaps between a dendrite's branches, its dipoles exhibit lesser near-field interactions than those in a plate. When illuminated by incident horizontal (vertical) polarization radiation, constructive (destructive) interference of neighboring dipoles' electric fields leads to enhanced Z_{DR} for horizontally oriented planar crystals (e.g., Lu et al. 2013).

2015 case). Regions of ascent were found to slope upward or downward in time, passing through different temperature levels and subsequently leading to various crystal habits at the surface. Coupled with thermodynamic information, such radar-based inferences of mesoscale ascent could substantially improve real-time estimates of SLRs (Roebber et al. 2003).

Together, these observations demonstrate that kinematic, thermodynamic, and microphysical processes conspire for the production of heavy snow. Yet, the different radar variables do not always evolve consistently, showing some degree of decoupling (e.g., between changes in low-level thermodynamics and those of the free troposphere aloft). This suggests that QVPs of the individual radar variables provide independent information and thus are valuable. Additionally, vertical gradients of these variables represent microphysical "fingerprints" (Kumjian 2012) of specific processes (e.g., aggregation is revealed by large Z_H increases toward the ground). In contrast to the qualitative information provided by hydrometeor identification algorithms, these fingerprints have intrinsic magnitudes associated with them, which could prove useful for *quantifying* microphysical processes.

Signatures previously identified in studies of the 8–9 February 2013 storm (Griffin et al. 2014; Picca et al. 2014) are found to be common in the storms analyzed herein. The repeatability of these signatures suggests they are common in northeastern U.S. winter cyclones. Additionally, the signatures observed in previous studies utilizing traditional PPI scans and reconstructed vertical cross sections are detectable using QVPs, demonstrating the utility of this technique for gaining microphysical and kinematic insights. This reliability also suggests that QVPs may provide some limited thermodynamic and kinematic information for model validation. Direct comparisons between radar observations and short-term numerical weather prediction model guidance could help operational meteorologists assess the confidence in particular model solutions, especially for ensemble predictions. The cases presented herein revealed examples of model error (disagreements between radar and model analyses). As in Griffin et al. (2014), we find cases (e.g., 5–6 March 2015) in which the RAP analyses fail to capture the evolution of the low-level thermodynamic profile, as evidenced by disagreements between the model-analyzed >0°C regions and the radar-observed melting layer. Additionally, several cases demonstrated radar-inferred and RAP-analyzed ascent maxima offset in time and space. In the absence of representative radiosonde and vertical velocity observations, polarimetric radar data could be useful for identifying these instances of model error. Layers of quasigeostrophic ascent implied by veering winds in the observed soundings, when available, are roughly consistent with these radar-retrieved ascent regions. Although an admittedly crude comparison, these results are encouraging and could point to providing such kinematic information between operational sounding times.

The link between kinematics, thermodynamics, and microphysical signatures observable with dual-polarization radar could be of value for data assimilation efforts. For example, Z_{DR} enhancements and large Z_H gradients are clearly and consistently observed near the -15°C isotherm. Additionally, melting signatures are thermodynamically constrained to occur where the wet-bulb temperature is ≥ 0°C. Doppler velocity QVPs provide some insights into broad (i.e., at the spatial scale of mesoscale numerical models) ascent. With sufficient validation in a large number of cases, it may be possible to assimilate such observations to improve model analyses. This differs from previous dual-polarization radar data assimilation efforts that focus on informing model microphysical fields (e.g., Jung et al. 2008a,b; Li and Mecikalski 2012).

Though the QVPs reveal bulk microphysical and kinematic structures in the storms presented herein, they are unable to provide insights into finescale structures such as shallow coastal fronts (e.g., Bosart et al. 1972; Marks and Austin 1979; Nielsen and Neilley 1990) and generating cells (e.g., Kumjian et al. 2014; Plummer et al. 2014; Rauber et al. 2014) that may be important for locally enhancing precipitation. This is especially true at higher altitudes, where averaging occurs over circles of progressively larger radii. To understand such finescale structures, finescale measurements are needed. Future work should incorporate high-resolution observations combined with in situ data together with detailed modeling studies to validate inferences from the radar observations presented herein and to better understand the links between thermodynamic and microphysical processes contributing to heavy snowfall and other hazards associated with northeastern U.S. coastal winter storms.

Acknowledgments. We thank Karen Kosiba, Josh Wurman, and Jim Marquis (Center for Severe Weather Research), as well as Mike French (Stony Brook University), for useful discussions. Joseph Picca (University of Oklahoma) suggested using METAR reports. Robert Schrom (The Pennsylvania State University) is thanked for assistance reading in RAP model analysis data and

for obtaining mPING reports. This work is partially supported by NSF Grant AGS-1143948. Brian Colle (Stony Brook University) and three additional anonymous reviewers are thanked for their comments and criticisms on the manuscript.

APPENDIX

QVPs of Doppler Velocity

Ryzhkov et al. (2016) present an overview and examples of the quasi-vertical profile (QVP) technique for viewing and analyzing polarimetric radar data. However, these authors did not consider Doppler velocity V_R in their description of QVPs. Some quantitatively useful information about the net mesoscale vertical motion in widespread precipitation is available from V_R QVPs. This appendix reviews the theory underpinning the physical interpretations of Doppler velocity QVPs.

The interpretation of V_R QVPs stems from work on velocity–azimuth displays (VADs; e.g., Lhermitte and Atlas 1961; Caton 1963; Browning and Wexler 1968; see also Doviak and Zrnić 1993). More sophisticated treatments of VADs and extensions to improve the accuracy of wind retrievals can be found in more recent literature (e.g., Waldteufel and Corbin 1979; Srivastava et al. 1986; Matejka and Srivastava 1991; Rauber et al. 1994; Mapes and Lin 2005). Given that the QVP technique utilizes a single elevation-angle scan, we restrict our focus to this framework for now, understanding that this limits the ability to assess the assumption of horizontal wind linearity and may be prone to errors when large horizontal wind nonlinearities exist within the conical volume scan. Future work should improve on this technique by using least squares regression on data from multiple elevation angles (e.g., Srivastava et al. 1986; Matejka and Srivastava 1991) to minimize the impact of noise on estimates of horizontal divergence. Comparison of QVP divergence retrievals at different elevation angles can be used to identify possible errors; it should be noted that for the cases shown herein, the QVPs were very consistent between different elevation angles (Fig. A1), except perhaps within the lowest ~1 km AGL, where biases from ground clutter and horizontal wind inhomogeneities are more common in winter storms.

Following geometrical considerations (e.g., Doviak and Zrnić 1993), the radial velocity V_R of a target relative to a radar pointing at elevation angle θ_e and azimuthal angle ϕ can be given as

$$V_R = u\sin\phi\cos\theta_e + v\cos\phi\cos\theta_e + w\sin\theta_e, \quad \text{(A1)}$$

where u, v, and w are components of the target's motion[A1] in the x, y, and z directions. We may write the horizontal wind field as a Taylor series about a point (x_0, y_0, z_0) in the radar domain:

$$u(x,y,z) = u_0 + (x-x_0)\frac{\partial u}{\partial x} + (y-y_0)\frac{\partial u}{\partial y} + (z-z_0)\frac{\partial u}{\partial z} + \text{h.o.t.} \quad \text{and} \quad \text{(A2)}$$

$$v(x,y,z) = v_0 + (x-x_0)\frac{\partial v}{\partial x} + (y-y_0)\frac{\partial v}{\partial y} + (z-z_0)\frac{\partial v}{\partial z} + \text{h.o.t.}, \quad \text{(A3)}$$

where h.o.t. represents higher-order terms and subscript 0 indicates the wind components at the point (x_0, y_0, z_0). Assuming the wind varies linearly across the domain of interest, we may ignore the higher-order terms. For data collected at constant θ_e and range (corresponding to a circle of constant altitude), we relax the linearity restriction for vertical variations in the wind (e.g., Browning and Wexler 1968; Doviak and Zrnić 1993). Note that each range gate is averaged independently in this study. Thus, components of the horizontally linear wind valid at a point above the radar ($x_0 = 0$, $y_0 = 0$, $z = z_0$) can be retrieved. If we substitute (A3) and (A2) into (A1), and realize that $x = r\sin\phi$ and $y = r\cos\phi$, where r is the ground-relative range from the radar, then we obtain

$$V_R = u_0\sin\phi\cos\theta_e + \frac{\partial u}{\partial x} r\sin^2\phi\cos\theta_e + \frac{\partial u}{\partial y} r\cos\phi\sin\phi\cos\theta_e + v_0\cos\phi\cos\theta_e + \frac{\partial v}{\partial x} r\sin\phi\cos\phi\cos\theta_e + \frac{\partial v}{\partial y} r\cos^2\phi\cos\theta_e + w\sin\theta_e. \quad \text{(A4)}$$

After making use of the following trig identities,

$$\sin^2\phi = \frac{1}{2} - \frac{1}{2}\cos(2\phi),$$

$$\cos^2\phi = \frac{1}{2} + \frac{1}{2}\cos(2\phi), \quad \text{and}$$

$$\sin\phi\cos\phi = \frac{1}{2}\sin(2\phi),$$

and some algebra and rearrangement of terms, we arrive at

[A1] Target horizontal motion is assumed equivalent to the horizontal wind, whereas its vertical motion w is the sum of its fall speed and vertical air motion.

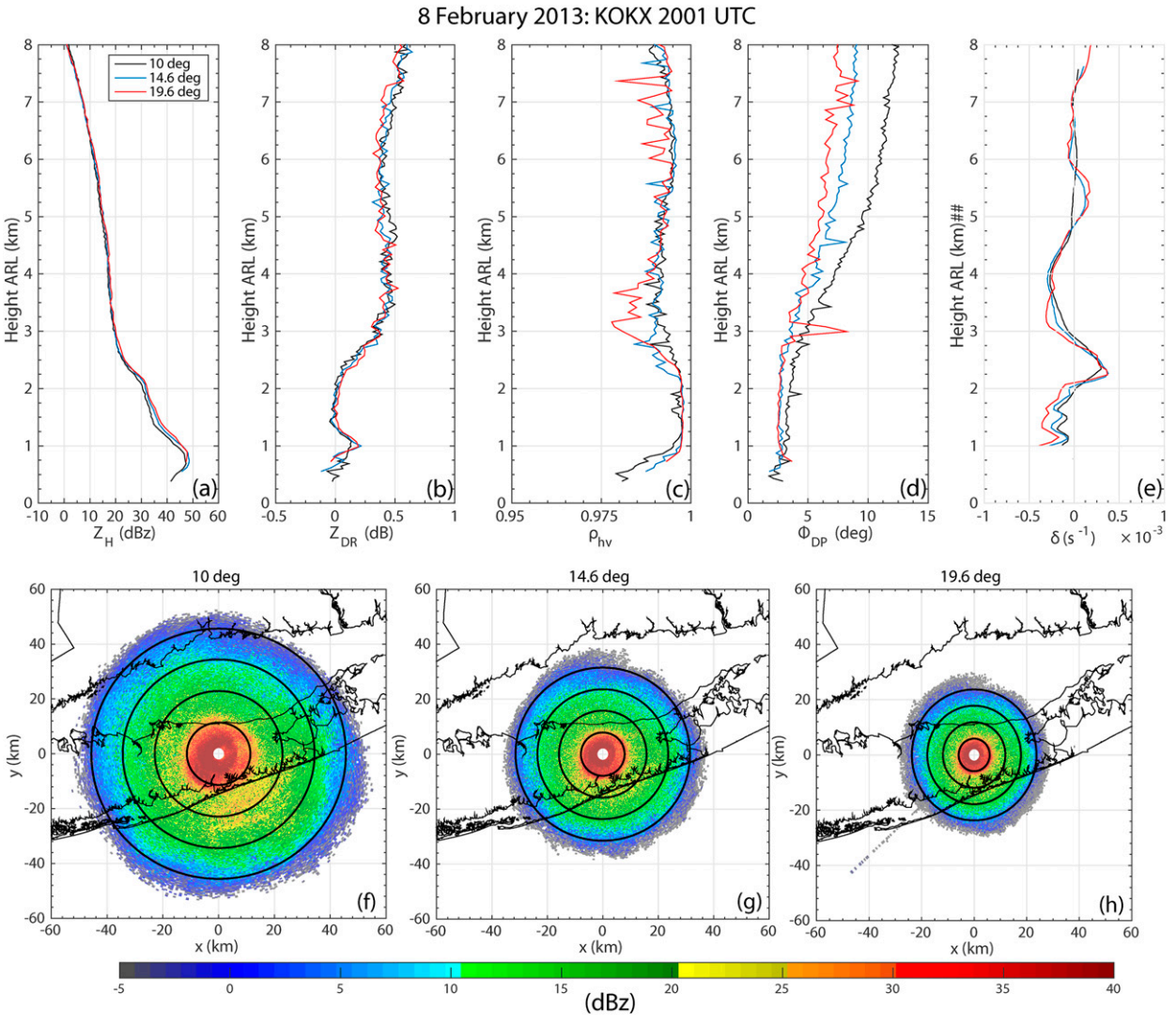

FIG. A1. Overlay of QVPs taken at three elevation angles (10° in black, 14.6° in blue, and 19.5° in red) for (a) Z_H, (b) Z_{DR}, (c) ρ_{hv}, (d) Φ_{DP}, and (e) $\bar{\delta}$ at 2001 UTC 8 Feb 2013, taken by KOKX. Profiles below 1 km ARL correspond to rain and thus are censored in (e). (f)–(h) The Z_H PPI corresponding to 10°, 14.6°, and 19.5° elevation angles, respectively.

$$V_R = u_0 \sin\phi \cos\theta_e + v_0 \cos\phi \cos\theta_e + \frac{1}{2} r \cos\theta_e \left(\frac{\partial u}{\partial x} + \frac{\partial v}{\partial y}\right) + \frac{1}{2} r \cos\theta_e \left(\frac{\partial v}{\partial y} - \frac{\partial u}{\partial x}\right) \cos(2\phi) + \frac{1}{2} r \cos\theta_e \left(\frac{\partial u}{\partial y} + \frac{\partial v}{\partial x}\right) \sin(2\phi) + w \sin\theta_e . \quad \text{(A5)}$$

The derivatives grouped in parentheses on the right-hand side of (A5) represent horizontal divergence $\overline{\delta} = \partial u/\partial x + \partial v/\partial y$, stretching deformation $\overline{D_1} = \partial u/\partial x - \partial v/\partial y$, and shearing deformation $\overline{D_2} = \partial u/\partial y + \partial v/\partial x$, where overbars indicate quantities averaged across the domain.

For a horizontally linear wind field, (A5) may be expressed as a Fourier series (following Browning and Wexler 1968):

$$V_R = \frac{1}{2} a_0 + \sum_{n=1}^{\infty} [a_n \cos(n\phi) + b_n \sin(n\phi)], \quad \text{(A6)}$$

where the Fourier coefficients are

$$a_0 = \overline{\delta} r \cos\theta_e + 2w \sin\theta_e ,$$

$$a_1 = u_0 \cos\theta_e,$$
$$a_2 = -\frac{1}{2}\overline{D_1} r \cos\theta_e,$$
$$b_1 = v_0 \cos\theta_e,$$
$$b_2 = \frac{1}{2}\overline{D_2} r \cos\theta_e, \quad \text{and}$$
$$a_3, \ldots, a_\infty = b_3, \ldots, b_\infty = 0.$$

Within the QVP framework, radar data are azimuthally averaged over 360° (2π):

$$\langle V_R \rangle = \frac{1}{2\pi} \int_0^{2\pi} V_R(\phi)\, d\phi.$$

Using the Fourier series (A6) for $V_R(\phi)$, we immediately see *all of the periodic functions average to zero*, leaving only

$$\langle V_R \rangle = \frac{1}{2} a_0 = \frac{1}{2} \overline{\delta} r \cos\theta_e + w \sin\theta_e. \tag{A7}$$

Thus, the measured $\langle V_R \rangle$ in the QVP contains information about the averaged horizontal divergence plus the averaged vertical motion of scatterers (Doviak and Zrnić 1993). *This assumption is only valid if no data are missing.* In this study, then, QVP V_R and $\overline{\delta}$ fields are censored if echoes are missing at any of the 360° azimuths at each height and time when averaging. Further, Doppler velocity data are dealiased prior to averaging to prevent spurious values.

For small r (close to the radar), we can approximate

$$r \approx h \frac{\cos\theta_e}{\sin\theta_e}, \tag{A8}$$

where h is the height of the beam above the ground. Therefore,

$$\langle V_R \rangle = \frac{1}{2} \overline{\delta} h \frac{\cos^2\theta_e}{\sin\theta_e} + w \sin\theta_e. \tag{A9}$$

Hydrometeor fall speed is expected to dominate vertical motion w because large *average* vertical air motions are not expected at scales over which averaging takes place. For small fall speeds typical of snow, and at 10° elevation, the fall speed contribution to the measured average Doppler velocity is very small: ~0.1–0.2 m s^{-1}. Thus, for the 10° elevation angle used in this study, the divergence term is dominant over the vertical motion term in (A9).

Thus, in the V_R QVPs, net convergence (divergence) is observed as negative (positive) values. Subsequently, ascent and descent are implied by convergence–divergence vertical dipole patterns. Note that QVP V_R magnitudes are amplified aloft owing to radar geometry [(A9)]. At farther ranges (corresponding to larger heights), the averaging takes place over a larger area. Thus, nonzero V_R QVP values aloft will be inflated relative to those at lower altitudes. The estimated divergence fields shown herein assume hydrometeor fall speeds are 1 m s^{-1} everywhere because we are focusing mainly on snowstorms; however, spuriously large convergence estimates are possible at low levels in rain. More sophisticated treatments of hydrometeor fall speed will be left for future work.

REFERENCES

Andrić, J., M. R. Kumjian, D. S. Zrnić, J. M. Straka, and V. M. Melnikov, 2013: Polarimetric signatures above the melting layer in winter storms: An observational and modeling study. *J. Appl. Meteor. Climatol.*, **52**, 682–700, doi:10.1175/JAMC-D-12-028.1.

Auer, A. H., and J. M. White, 1982: The combined role of kinematics, thermodynamics and cloud physics associated with heavy snowfall episodes. *J. Meteor. Soc. Japan*, **60**, 500–507.

Bailey, M. P., and J. Hallett, 2009: A comprehensive habit diagram for atmospheric ice crystals: Confirmation from the laboratory, AIRS II, and other field studies. *J. Atmos. Sci.*, **66**, 2888–2899, doi:10.1175/2009JAS2883.1.

Bechini, R., L. Baldini, and V. Chandrasekar, 2013: Polarimetric radar observations of the ice region of precipitation clouds at C-band and X-band radar frequencies. *J. Appl. Meteor. Climatol.*, **52**, 1147–1169, doi:10.1175/JAMC-D-12-055.1.

Benjamin, S. G., and Coauthors, 2004: An hourly assimilation–forecast cycle: The RUC. *Mon. Wea. Rev.*, **132**, 495–518, doi:10.1175/1520-0493(2004)132<0495:AHACTR>2.0.CO;2.

Bluestein, H. B., 1992: *Principles of Kinematics and Dynamics*. Vol. 1, *Synoptic–Dynamic Meteorology in Midlatitudes*, Oxford University Press, 431 pp.

Bohren, C. F., and D. R. Huffman, 1983: *Absorption and Scattering of Light by Small Particles.* 2d ed. John Wiley and Sons, 530 pp.

Bosart, L. F., C. J. Vaudo, and J. H. Helsdon, 1972: Coastal frontogenesis. *J. Appl. Meteor.*, **11**, 1236–1258, doi:10.1175/1520-0450(1972)011<1236:CF>2.0.CO;2.

Brennan, M. J., and G. M. Lackmann, 2005: The influence of incipient latent heat release on the precipitation distribution of the 24–25 January 2000 U.S. East Coast cyclone. *Mon. Wea. Rev.*, **133**, 1913–1937, doi:10.1175/MWR2959.1.

Bringi, V. N., and V. Chandrasekar, 2001: *Polarimetric Doppler Weather Radar.* Cambridge University Press, 636 pp.

Browning, K. A., 1971: Radar measurements of air motion near fronts. *Weather*, **26**, 320–340, doi:10.1002/j.1477-8696.1971.tb04211.x.

——, and R. Wexler, 1968: The determination of kinematic properties of a wind field using Doppler radar. *J. Appl. Meteor.*, **7**, 105–113, doi:10.1175/1520-0450(1968)007<0105:TDOKPO>2.0.CO;2.

Carlson, T. N., 1980: Airflow through midlatitude cyclones and the comma cloud pattern. *Mon. Wea. Rev.*, **108**, 1498–1509, doi:10.1175/1520-0493(1980)108<1498:ATMCAT>2.0.CO;2.

Caton, P. G. F., 1963: The measurement of wind and convergence by Doppler radar. Preprints, *10th Conf. on Radar Meteorology*, Washington, DC, Amer. Meteor. Soc., 290–296.

Colle, B. A., D. Stark, and S. E. Yuter, 2014: Surface microphysical observations within East Coast winter storms on Long Island, New York. *Mon. Wea. Rev.*, **142**, 3126–3146, doi:10.1175/MWR-D-14-00035.1.

Davis, C. A., 1992: A potential-vorticity diagnosis of the importance of initial structure and condensational heating in observed extratropical cyclogenesis. *Mon. Wea. Rev.*, **120**, 2409–2428, doi:10.1175/1520-0493(1992)120<2409:APVDOT>2.0.CO;2.

Dokoupil, T., 2015: How National Weather Service cost East Coast millions. NBC News. [Available online at: http://www.nbcnews.com/storyline/blizzard-15/how-national-weather-service-cost-east-coast-millions-n297031.]

Doviak, R. J., and D. S. Zrnić, 1993: *Doppler Radar and Weather Observations.* 2d ed. Academic Press, 562 pp.

Elmore, K. L., Z. L. Flaming, V. Lakshmanan, B. T. Kaney, V. Farmer, H. D. Reeves, and L. P. Rothfusz, 2014: mPING: Crowd-sourcing weather reports for research. *Bull. Amer. Meteor. Soc.*, **95**, 1335–1342, doi:10.1175/BAMS-D-13-00014.1.

Ganetis, S., and B. A. Colle, 2015: The thermodynamic and microphysical evolution of an intense snowbound during the northeast U.S. blizzard of 8–9 February 2013. *Mon. Wea. Rev.*, **143**, 4104–4125, doi:10.1175/MWR-D-14-00407.1.

Griffin, E. M., T. J. Schuur, A. V. Ryzhkov, H. D. Reeves, and J. C. Picca, 2014: A polarimetric and microphysical investigation of the northeast blizzard of 8–9 February 2013. *Wea. Forecasting*, **29**, 1271–1294, doi:10.1175/WAF-D-14-00056.1.

Hallett, J., and S. C. Mossop, 1974: Production of secondary ice crystals during the riming process. *Nature*, **249**, 26–28, doi:10.1038/249026a0.

Jung, Y., G. Zhang, and M. Xue, 2008a: Assimilation of simulated polarimetric radar data for a convective storm using the ensemble Kalman filter. Part I: Observation operators for reflectivity and polarimetric variables. *Mon. Wea. Rev.*, **136**, 2228–2245, doi:10.1175/2007MWR2083.1.

——, M. Xue, G. Zhang, and J. M. Straka, 2008b: Assimilation of simulated polarimetric radar data for a convective storm using the ensemble Kalman filter. Part II: Impact of polarimetric data on storm analysis. *Mon. Wea. Rev.*, **136**, 2246–2260, doi:10.1175/2007MWR2288.1.

Kennedy, P. C., and S. A. Rutledge, 2011: S-band dual-polarization radar observations of winter storms. *J. Appl. Meteor. Climatol.*, **50**, 844–858, doi:10.1175/2010JAMC2558.1.

Kocin, P. J., and L. W. Uccellini, 2004: *Overview.* Vol. 1, *Northeast Snowstorms*, *Meteor. Monogr.*, No. 54, Amer. Meteor. Soc., 296 pp.

Kumjian, M. R., 2012: The impact of precipitation physical processes on the polarimetric radar variables. Ph.D. dissertation, University of Oklahoma, 248 pp.

——, 2013a: Principles and applications of dual-polarization weather radar. Part I: Description of the polarimetric radar variables. *J. Oper. Meteor.*, **1**, 226–242, doi:10.15191/nwajom.2013.0119.

——, 2013b: Principles and applications of dual-polarization weather radar. Part II: Warm and cold season applications. *J. Oper. Meteor.*, **1**, 243–264, doi:10.15191/nwajom.2013.0120.

——, 2013c: Principles and applications of dual-polarization weather radar. Part III: Artifacts. *J. Oper. Meteor.*, **1**, 265–274, doi:10.15191/nwajom.2013.0121.

——, A. V. Ryzhkov, H. D. Reeves, and T. J. Schuur, 2013: A dual-polarization radar signature of hydrometeor refreezing in winter storms. *J. Appl. Meteor. Climatol.*, **52**, 2549–2566, doi:10.1175/JAMC-D-12-0311.1.

——, S. A. Rutledge, R. M. Rasmussen, P. C. Kennedy, and M. Dixon, 2014: High-resolution polarimetric radar observations of snow-generating cells. *J. Appl. Meteor. Climatol.*, **53**, 1636–1658, doi:10.1175/JAMC-D-13-0312.1.

——, S. Mishra, S. E. Giangrande, T. Toto, A. V. Ryzhkov, and A. Bansemer, 2016: Polarimetric radar and aircraft observations of saggy bright bands during MC3E. *J. Geophys. Res. Atmos.*, **121**, 3584–3607, doi:10.1002/2015JD024446.

Kuo, Y.-H., and R. J. Reed, 1988: Numerical simulation of an explosively deepening cyclone in the eastern Pacific. *Mon. Wea. Rev.*, **116**, 2081–2105, doi:10.1175/1520-0493(1988)116<2081:NSOAED>2.0.CO;2.

Lamb, D., and J. Verlinde, 2011: *Physics and Chemistry of Clouds.* Cambridge University Press, 584 pp.

Lhermitte, R. M., and D. Atlas, 1961: Precipitation motion by pulse-Doppler radar. Preprints, *Ninth Conf. on Radar Meteorology*, Kansas City, MO, Amer. Meteor. Soc., 218–223.

Li, X., and J. R. Mecikalski, 2012: Impact of the dual-polarization Doppler radar data on two convective storms with a warm-rain radar forward operator. *Mon. Wea. Rev.*, **140**, 2147–2167, doi:10.1175/MWR-D-11-00090.1.

Lombardo, K. A., B. A. Colle, and Z. Zhang, 2015: Evaluation of historical and future cool season precipitation over the eastern United States and western Atlantic storm track using CMIP5 models. *J. Climate*, **28**, 451–467, doi:10.1175/JCLI-D-14-00343.1.

Lu, Y., E. E. Clothiaux, K. Aydin, G. Botta, and J. Verlinde, 2013: Modeling variability in dendritic ice crystal backscattering cross sections at millimeter wavelengths using a modified Rayleigh–Gans theory. *J. Quant. Spectrosc. Radiat. Transfer*, **131**, 95–104, doi:10.1016/j.jqsrt.2013.05.008.

Mapes, B. E., and J. Lin, 2005: Doppler radar observations of mesoscale wind divergence in regions of tropical convection. *Mon. Wea. Rev.*, **133**, 1808–1824, doi:10.1175/MWR2941.1.

Marks, F. D., Jr., and P. M. Austin, 1979: Effects of the New England coastal front on the distribution of precipitation. *Mon. Wea. Rev.*, **107**, 53–67, doi:10.1175/1520-0493(1979)107<0053:EOTNEC>2.0.CO;2.

Matejka, T., and R. C. Srivastava, 1991: An improved version of the extended velocity–azimuth display analysis of single-Doppler radar data. *J. Atmos. Oceanic Technol.*, **8**, 453–466, doi:10.1175/1520-0426(1991)008<0453:AIVOTE>2.0.CO;2.

Melnikov, V. M., 2004: Simultaneous transmission mode for the polarimetric WSR-88D. National Severe Storms Laboratory Rep., 84 pp. [Available online at http://www.nssl.noaa.gov/publications/wsr88d_reports/SHV_statistics.pdf.]

Moisseev, D., E. Saltikoff, and M. Leskinen, 2009: Dual-polarization weather radar observations of snow growth processes. *34th Conf. on Radar Meteorology*, Williamsburg, VA, Amer. Meteor. Soc., 13B.2 [Available online at http://ams.confex.com/ams/pdfpapers/156123.pdf.]

——, S. Lautaportti, J. Tyynela, and S. Lim, 2015: Dual-polarization radar signatures in snowstorms: Role of snowflake aggregation. *J. Geophys. Res. Atmos.*, **120**, 12 644–12 655, doi:10.1002/2015JD023884.

Nelson, J., and C. Knight, 1998: Snow crystal habit changes explained by layer nucleation. *J. Atmos. Sci.*, **55**, 1452–1465, doi:10.1175/1520-0469(1998)055<1452:SCHCEB>2.0.CO;2.

Nielsen, J. W., and P. P. Neilley, 1990: The vertical structure of New England coastal fronts. *Mon. Wea. Rev.*, **118**, 1793–1807, doi:10.1175/1520-0493(1990)118<1793:TVSONE>2.0.CO;2.

Novak, D. R., B. A. Colle, and R. McTaggart-Cowan, 2009: The role of moist processes in the formation and evolution of mesoscale snowbands within the comma head of a northeast U.S. cyclone. *Mon. Wea. Rev.*, **137**, 2662–2686, doi:10.1175/2009MWR2874.1.

Otto, R., 2015: Mid-Atlantic to northeast major winter storm 26–28 January 2015. WPC Event Summary, 3 pp. [Available online

at http://www.wpc.ncep.noaa.gov/winter_storm_summaries/event_reviews/2015/MidAtlantic_Northeast_Major_WinterStorm_Jan2015.pdf.]

Oue, M., M. Galletti, J. Verlinde, A. Ryzhkov, and Y. Lu, 2016: Use of X-band differential reflectivity measurements to study shallow Arctic mixed-phase clouds. *J. Appl. Meteor. Climatol.*, **55**, 403–424, doi:10.1175/JAMC-D-15-0168.1.

Peters, G., B. Fischer, and T. Andersson, 2002: Rain observations with a vertically looking Micro Rain Radar (MRR). *Bor. Environ. Res.*, **7**, 353–362.

Picca, J. C., D. M. Schultz, B. A. Colle, S. Gannets, D. Novak, and M. J. Sienkiewicz, 2014: The value of dual-polarization radar in diagnosing the complex microphysical evolution of an intense snowband. *Bull. Amer. Meteor. Soc.*, **95**, 1825–1834, doi:10.1175/BAMS-D-13-00258.1.

Plummer, D. M., G. M. McFarquhar, R. M. Rauber, B. F. Jewett, and D. C. Leon, 2014: Structure and statistical analysis of the microphysical properties of generating cells in the comma head region of continental winter cyclones. *J. Atmos. Sci.*, **71**, 4181–4203, doi:10.1175/JAS-D-14-0100.1.

Posselt, D. J., and J. E. Martin, 2004: The effect of latent heat release on the evolution of a warm occluded thermal structure. *Mon. Wea. Rev.*, **132**, 578–599, doi:10.1175/1520-0493(2004)132<0578:TEOLHR>2.0.CO;2.

Rauber, R. M., M. K. Ramamurthy, and A. Tokay, 1994: Synoptic and mesoscale structure of a severe freezing rain event: The Valentine's Day ice storm. *Wea. Forecasting*, **9**, 183–208, doi:10.1175/1520-0434(1994)009<0183:SAMSOA>2.0.CO;2.

——, and Coauthors, 2014: Stability and charging characteristics of the comma head region of continental winter cyclones. *J. Atmos. Sci.*, **71**, 1559–1582, doi:10.1175/JAS-D-13-0253.1.

Roebber, P. J., S. L. Bruening, D. M. Schultz, and J. V. Cortinas, 2003: Improving snowfall forecasting by diagnosing snow density. *Wea. Forecasting*, **18**, 264–287, doi:10.1175/1520-0434(2003)018<0264:ISFBDS>2.0.CO;2.

Ryerson, C. C., and A. C. Ramsay, 2007: Quantitative ice accretion information from the Automated Surface Observing System. *J. Appl. Meteor. Climatol.*, **46**, 1423–1437, doi:10.1175/JAM2535.1.

Ryzhkov, A. V., T. J. Schuur, D. W. Burgess, P. L. Heinselman, S. E. Giangrande, and D. S. Zrnić, 2005: The Joint Polarization Experiment: Polarimetric rainfall measurements and hydrometeor classification. *Bull. Amer. Meteor. Soc.*, **86**, 809–824, doi:10.1175/BAMS-86-6-809.

——, P. Zhang, H. D. Reeves, M. R. Kumjian, T. Tschallener, S. Trömel, and C. Simmer, 2016: Quasi-vertical profiles—A new way to look at polarimetric radar data. *J. Atmos. Oceanic Technol.*, **33**, 551–562, doi:10.1175/JTECH-D-15-0020.1.

Sanders, F., and J. R. Gyakum, 1980: Synoptic-dynamic climatology of the "bomb." *Mon. Wea. Rev.*, **108**, 1589–1606, doi:10.1175/1520-0493(1980)108<1589:SDCOT>2.0.CO;2.

Schneebeli, M., N. Dawes, M. Lehning, and A. Berne, 2013: High-resolution vertical profiles of X-band polarimetric radar observables during snowfall in the Swiss Alps. *J. Appl. Meteor. Climatol.*, **52**, 378–394, doi:10.1175/JAMC-D-12-015.1.

Schrom, R. S., and M. R. Kumjian, 2016: Connecting microphysical processes in Colorado winter storms with vertical profiles of radar variables. *J. Appl. Meteor. Climatol.*, **55**, 1771–1787, doi:10.1175/JAMC-D-15-0338.1.

——, ——, and Y. Lu, 2015: Polarimetric radar signatures of dendritic growth zones within Colorado winter storms. *J. Appl. Meteor. Climatol.*, **54**, 2365–2388, doi:10.1175/JAMC-D-15-0004.1.

Srivastava, R. C., T. J. Matejka, and T. J. Lorello, 1986: Doppler radar study of the trailing anvil region associated with a squall line. *J. Atmos. Sci.*, **43**, 356–377, doi:10.1175/1520-0469(1986)043<0356:DRSOTT>2.0.CO;2.

Stark, D., B. A. Colle, and S. E. Yuter, 2013: Observed microphysical evolution for two East Coast winter storms and the associated snow bands. *Mon. Wea. Rev.*, **141**, 2037–2057, doi:10.1175/MWR-D-12-00276.1.

Sulia, K. J. and J. Y. Harrington, 2011: Ice ascent ratio influences on mixed-phase clouds: Impacts on phase partitioning in parcel models. *J. Geophys. Res.*, **116**, D21309, doi:10.1029/2011JD016298.

Takahashi, T., T. Endoh, and G. Wakahama, 1991: Vapor diffusional growth of free-falling snow crystals between −3 and −23°C. *J. Meteor. Soc. Japan*, **69**, 15–30.

Thompson, E. J., S. A. Rutledge, B. Dolan, V. Chandrasekar, and B. L. Cheong, 2014: A dual-polarization radar hydrometeor classification algorithm for winter precipitation. *J. Atmos. Oceanic Technol.*, **31**, 1457–1481, doi:10.1175/JTECH-D-13-00119.1.

Trömel, S., M. R. Kumjian, A. V. Ryzhkov, C. Simmer, and M. Diederich, 2013: Backscatter differential phase—Estimation and variability. *J. Appl. Meteor. Climatol.*, **52**, 2529–2548, doi:10.1175/JAMC-D-13-0124.1.

——, A. V. Ryzhkov, P. Zhang, and C. Simmer, 2014: Investigations of backscatter differential phase in the melting layer. *J. Appl. Meteor. Climatol.*, **53**, 2344–2359, doi:10.1175/JAMC-D-14-0050.1.

Van den Broeke, M. S., D. M. Tobin, and M. R. Kumjian, 2016: Polarimetric radar observations of precipitation type and rate from the 2–3 March 2014 winter storm in Oklahoma and Arkansas. *Wea. Forecasting*, **31**, 1179–1196, doi:10.1175/WAF-D-16-0011.1.

Vogel, J. M., F. Fabry, and I. Zawadzki, 2015: Attempts to observe polarimetric signatures of riming in stratiform precipitation. *37th Conf. on Radar Meteorology*, Norman, OK, Amer. Meteor. Soc., 6B.6. [Available online at https://ams.confex.com/ams/37RADAR/webprogram/Paper275246.html.]

Waldteufel, P., and H. Corbin, 1979: On the analysis of single-Doppler radar data. *J. Appl. Meteor.*, **18**, 532–542, doi:10.1175/1520-0450(1979)018<0532:OTAOSD>2.0.CO;2.

Zawadzki, I., 2013: Observations of snow growth by a vertically pointing radar. *36th Conf. on Radar Meteorology*, Breckenridge, CO, Amer. Meteor. Soc., 11A.6 [Available online at https://ams.confex.com/ams/36Radar/webprogram/Paper229071.html.]

Zrnić, D. S., and A. V. Ryzhkov, 1999: Polarimetry for weather surveillance radars. *Bull. Amer. Meteor. Soc.*, **80**, 389–406, doi:10.1175/1520-0477(1999)080<0389:PFWSR>2.0.CO;2.